



Active metamaterials for realizing odd mass density

Qian Wu^{a,1} , Xianchen Xu^{a,1}, Honghua Qian^{a,1}, Shaoyun Wang^a, Rui Zhu^b , Zheng Yan^a , Hongbin Ma^a , Yangyang Chen^{c,2}, and Guoliang Huang^{a,2}

Edited by John Rogers, Northwestern University, Evanston, IL; received June 9, 2022; accepted March 29, 2023

Solids built out of active components have exhibited odd elastic stiffness tensors whose active moduli appear in the antisymmetric part and which give rise to non-Hermitian static and dynamic phenomena. Here, we present a class of active metamaterial featured with an odd mass density tensor whose asymmetric part arises from active and nonconservative forces. The odd mass density is realized using metamaterials with inner resonators connected by asymmetric and programmable feed-forward control on acceleration and active forces along the two perpendicular directions. The active forces produce unbalanced off-diagonal mass density coupling terms, leading to non-Hermiticity. The odd mass is then experimentally validated through a one-dimensional nonsymmetric wave coupling where propagating transverse waves are coupled with longitudinal ones whereas the reverse is forbidden. We reveal that the two-dimensional active metamaterials with the odd mass can perform in either energy-unbroken or energy-broken phases separated by exceptional points along principal directions of the mass density. The odd mass density contributes to the wave anisotropy in the energy-unbroken phase and directional wave energy gain in the energy-broken phase. We also numerically illustrate and experimentally demonstrate the two-dimensional wave propagation phenomena that arise from the odd mass in active solids. Finally, the existence of non-Hermitian skin effect is discussed in which boundaries host an extensive number of localized modes. It is our hope that the emergent concept of the odd mass can open up a new research platform for mechanical non-Hermitian system and pave the ways for developing next-generation wave steering devices.

odd mass density | elastic metamaterial | non-Hermitian mechanical system | energy phase transition | non-Hermitian skin effect

Mechanical metamaterials have gained extensive attention in the last two decades due to their ability to exhibit material properties that are challenging to obtain in nature (1–5). Intensive research has been conducted in order to determine the basic physics behind these materials and their possible engineering applications. For example, various engineered materials with negative effective mass density and/or negative modulus were demonstrated for wave attenuation, noise reduction, wave focusing, and cloaking, where the mass density and stiffness tensors are essentially symmetric because of the system Hermiticity (6–20). Recent breakthroughs in active topological dynamics in the context of topological pumping and nonreciprocal wave propagation have motivated the search for topology-based wave functionalities by introducing active components into mechanical metamaterials, which are baptized as non-Hermitian systems (21–26).

The non-Hermitian mechanical systems made of active components for energetic interactions with the environment have opened perspectives for active material design. Significant efforts have been made in expanding conventional continuum mechanics to accommodate systems exhibiting odd elasticity with broken energy conservation laws, where the stiffness tensor is asymmetric (27–29). A material displaying odd elasticity must violate Maxwell–Betti reciprocity. This intriguing feature has recently been experimentally demonstrated by introducing piezoelectric elements and motors controlled by electrical circuits into host media (30–32). Additionally, these non-Hermitian systems with odd elasticity exhibit non-Hermitian skin effect in both one and two dimensions (1D and 2D). Recently, they were designed to perform basic robotic manipulations such as steering motion and forces (33). However, all the odd metamaterials and related nonconventional wave control are concentrated on odd elasticity and their related topological wave propagation.

Here, we report, design, and examine the non-Hermitian wave phenomena that arise from an active solid with odd mass density, where the mass density tensor appears to be asymmetric. An elastic metamaterial with inner resonators is equipped with piezoelectric elements mounted on supporting beams and controlled by electrical circuits to break reciprocity between the local acceleration and active forces along the two perpendicular

Significance

The conventional mechanical metamaterials with inner resonators are characterized as homogenized solids with symmetric effective mass density tensors to interpret subwavelength wave attenuation mechanism. In this work, we present a class of active metamaterials described by an odd mass density tensor which is no longer symmetric and whose nonzero asymmetric part arises from active and nonconservative forces. The unconventional wave phenomena caused by the odd mass density are demonstrated experimentally and numerically. The directional wave amplification is also illustrated by controllable feed-forward electric circuits. This finding may contribute to a wave manipulation strategy in nondestructive structural health monitoring, sensing, and vibration suppression and control.

Author contributions: Y.C. and G.H. designed research; Q.W., X.X., H.Q., S.W., Y.C., and G.H. performed research; Q.W., Y.C., and G.H. analyzed data; G.H. supervised the research; and Q.W., R.Z., Z.Y., H.M., Y.C., and G.H. wrote the paper.

The authors declare no competing interest.

This article is a PNAS Direct Submission.

Copyright © 2023 the Author(s). Published by PNAS. This article is distributed under Creative Commons Attribution-NonCommercial-NoDerivatives License 4.0 (CC BY-NC-ND).

¹Q.W., X.X., and H.Q. contributed equally to this work.

²To whom correspondence may be addressed. Email: maeychen@ust.hk or huangg@missouri.edu.

This article contains supporting information online at <https://www.pnas.org/lookup/suppl/doi:10.1073/pnas.2209829120/-DCSupplemental>.

Published May 18, 2023.

directions. Our approach enables nonsymmetric coupling between longitudinal and transverse motions in continuum solids. The odd mass density simultaneously breaks parity and Maxwell–Betti reciprocity. The active solid can perform energy phase transition between energy-unbroken and energy-broken phases separated by exceptional points, in analogy to the non-Hermitian parity-time-reversal (PT) symmetric systems with balanced gain and loss (34–36). We experimentally evidence 1D nonsymmetric wave coupling where only transverse waves can be coupled into longitudinal ones but not vice versa. 2D directional wave amplification associated with the energy phase transition is experimentally observed as well. Additionally, mechanical wave amplification and related non-Hermitian skin effect are also numerically demonstrated in 2D active solids. Our work paves an alternative way to realize a class of active solids and provides design guidelines for odd-density behaviors in active solids.

Odd Mass Density Tensors for Active Metamaterials. The 2D mechanical metamaterial with inner resonators periodically distributed in the matrix has been intensively investigated in the past decades for generating subwavelength bandgaps and their unconventional wave control abilities in elastic solids (37, 38), as shown in Fig. 1A. To understand the working mechanism, effective mass density properties of the metamaterial can be formulated by considering a mass-in-mass unit. For the passive 2D metamaterial (Fig. 1B), the equations of motions of the inner and outer masses can be easily obtained as

$$F_i + (u'_i - u_i) k_i = M \ddot{u}_i, \quad [1]$$

$$(u_i - u'_i) k_i = m \ddot{u}'_i, \quad [2]$$

where F_i is the external force applied on the outer mass $M = a^2 \rho^2$ in \mathbf{x}_i , u_i and u'_i are the displacements of the outer and inner masses along the \mathbf{x}_i direction, respectively. Substituting Eq. 2 into Eq. 1 subjected to harmonic forces, we readily obtain

$$F_i = -a^2 \hat{\rho}_{ij} \omega^2 u_j, \quad [3]$$

where

$$\hat{\rho}_{ij} = \begin{bmatrix} \hat{\rho}_{11}(\omega) & 0 \\ 0 & \hat{\rho}_{22}(\omega) \end{bmatrix}, \quad [4]$$

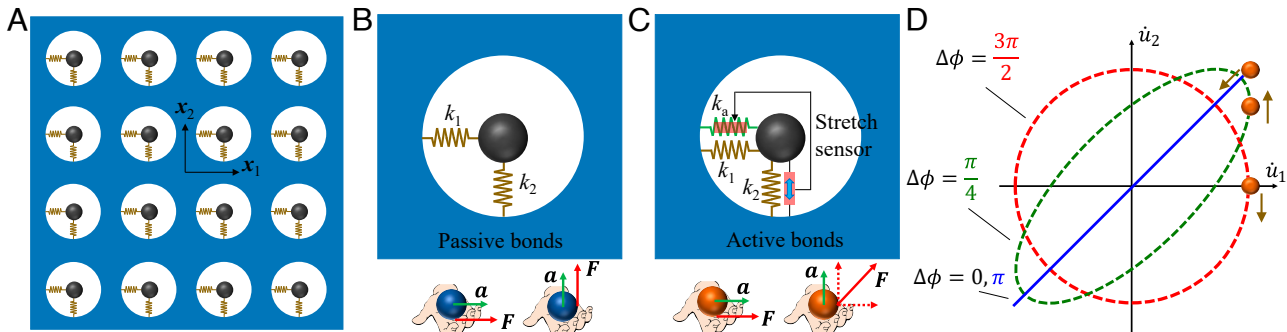


Fig. 1. (A) 2D elastic metamaterial enabled by inner resonators with a lattice size a . (B) Passive unit cell that carries conventional mass supports symmetric force-acceleration relationship: the accelerations align always with the resulting forces. In the unit cell, the inner (black) and outer (blue frame) masses are denoted as m and M , respectively. The Hookean bonds have spring constants k_1 and k_2 in the \mathbf{x}_1 and \mathbf{x}_2 directions. (C) Active unit cell that carries odd mass comes with asymmetric force-acceleration relationship: Orthogonal accelerations generate nonorthogonal forces, and the process is asymmetric. In addition to the Hookean k_1 and k_2 , the unit cell conceptually consists of a stretch strain sensor which measures $u'_2 - u_2$ in \mathbf{x}_2 and an active Hookean bond which generates an active force $F_a = (u'_2 - u_2)k_a$ in \mathbf{x}_1 . (D) Kinetic energy cycle of the odd mass with $\hat{\rho}_{12} \in \mathbb{R}$ and being positive. The particle indicates the velocity trajectory for each selected value of $\Delta\phi = \phi_1 - \phi_2$ from 0 to $2\pi/\omega$ (Eq. 8). Clockwise and counterclockwise trajectories of the particle encircle nonzero area on the map, indicate nonzero work done, and correspond to kinetic energy generated and lost, respectively.

is the effective mass density tensor of the metamaterial with $\hat{\rho}_{11}(\omega) = \frac{M}{a^2} + \frac{k_1 m}{a^2(k_1 - \omega^2 m)}$ and $\hat{\rho}_{22}(\omega) = \frac{M}{a^2} + \frac{k_2 m}{a^2(k_2 - \omega^2 m)}$. As noticed, for passive designs, the effective mass density tensor, $\hat{\rho}_{ij}$, is always symmetric, i.e., $\hat{\rho}_{12} = \hat{\rho}_{21}$, and the components, $\hat{\rho}_{11}$ and $\hat{\rho}_{22}$, can be positive or negative values depending on the operation frequency ω . For the unit with symmetric mass density tensor, the total work done by the external force is equal to the change of kinetic energy of the mass, which means that the mass itself neither injects nor dissipates kinetic energy. The passive metamaterial is then a classical Hermitian system.

Consider now an active unit by installing a stretch sensor to k_2 and a force actuator on top of k_1 (Fig. 1C). The sensed stretch $u'_2 - u_2$ is fed to the actuator using an active bond k_a . The active force generated by the active bond and applied on the outer mass along the \mathbf{x}_1 direction can be written as $F_a = (u'_2 - u_2)k_a$. Note that k_a is not necessary to be a real number. Instead, it can be a complex number leading to phase difference between the stretch and the force F_a for harmonic motions. As a matter of fact, the active bond builds a new relationship between the stretch and the perpendicular force, which is absent in passive units. In addition, the active bond is nonlocal, given that the stretch and the force are not at the same location. As a result, the active bond induces no feedback stretch in k_2 for infinitesimal deformations. The effect of the active bond is hence feed-forward. By adding the active bond into equations of motion given in Eqs. 1 and 2, the effective mass density tensor of the active unit can be obtained as

$$\hat{\rho}_{ij} = \begin{bmatrix} \hat{\rho}_{11}(\omega) & \hat{\rho}_{12}(\omega) \\ 0 & \hat{\rho}_{22}(\omega) \end{bmatrix}, \quad [5]$$

where the off-diagonal term

$$\hat{\rho}_{12} = -\frac{k_a \omega^2 m^2}{a^2(k_1 - \omega^2 m)(k_2 - \omega^2 m)}, \quad [6]$$

characterizes the relationship between the acceleration and the external force perpendicular to the acceleration. It can be easily seen that $\hat{\rho}_{12}$ is linearly controlled by the active bond k_a and regulated by the two resonance modes along the two perpendicular directions, as both the sensing and actuation are resonance dependent.

Interestingly, the effective mass density tensor of the active unit is asymmetric, $\hat{\rho}_{12} \neq \hat{\rho}_{21}$. In the design, the acceleration

along the \mathbf{x}_1 direction does not induce an external force along the \mathbf{x}_2 direction because no sensors along the \mathbf{x}_1 direction and no actuators along the \mathbf{x}_2 direction are placed, and the feedback from the active bond is absent. Consequently, $\hat{\rho}_{21} = 0$. It is useful to split $\hat{\rho}_{ij}$ into two tensors: a symmetric (even) mass density tensor, $\hat{\rho}_{ij}^e$, and an antisymmetric (odd) mass density tensor, $\hat{\rho}_{ij}^o$,

$$\hat{\rho}_{ij} = \hat{\rho}_{ij}^e + \hat{\rho}_{ij}^o = \begin{bmatrix} \hat{\rho}_{11} & \hat{\rho}_{12}^e \\ \hat{\rho}_{21}^e & \hat{\rho}_{22} \end{bmatrix} + \begin{bmatrix} 0 & \hat{\rho}_{12}^o \\ -\hat{\rho}_{12}^o & 0 \end{bmatrix}, \quad [7]$$

where $\hat{\rho}_{12}^e = \hat{\rho}_{21}^e = \hat{\rho}_{12}/2$. The even part of the mass density tensor, $\hat{\rho}_{12}^e$, modulates anisotropy of the effective mass density tensor in the active metamaterial. This can be understood by finding principal effective mass densities of $\hat{\rho}_{ij}^e$ along principal directions through rotational coordinate transformations. Thus, $\hat{\rho}_{12}^e$ is a parameter contributing to mass anisotropy of the active metamaterial.

The odd part of the mass density tensor, $\hat{\rho}_{12}^o$, demands a force always perpendicular to the acceleration. This is a direct consequence of the active bond that, under some conditions, can inject or dissipate energy into or from the active metamaterial. To see this characteristics, we assume $\hat{\rho}_{12}^o \in \mathbb{R}$, $\dot{u}_1 = \bar{v}_1 \sin(\omega t + \phi_1)$, and $\dot{u}_2 = \bar{v}_2 \sin(\omega t + \phi_2)$. The work done by the external force in one cycle of oscillations reads

$$W_F = \int_0^{2\pi/\omega} F_i^o \cdot \dot{u}_i dt = \int_0^{2\pi/\omega} a^2 \hat{\rho}_{12}^o \ddot{u}_i \dot{u}_j dt \\ = -2\pi a^2 \hat{\rho}_{12}^o \bar{v}_1 \bar{v}_2 \sin(\phi_1 - \phi_2). \quad [8]$$

On the other hand, the induced kinetic energy due to $\hat{\rho}_{ij}^o$ is always zero since $W_E = \frac{1}{2} a^2 \hat{\rho}_{ij}^o \dot{u}_i \dot{u}_j = 0$. If the internal dissipation of the active metamaterial is not considered, the condition $W_F + W_I = 0$ should be imposed for the balance of energy between work done by the external electric system and the total internal energy gain or loss of the metamaterial in one excitation cycle, where W_I is the total internal energy gain or loss caused by the active bond. In particular, when \dot{u}_1 and \dot{u}_2 are in-phase or out-of-phase, $W_F = W_I = 0$ and the active bond is in a silence mode without energy exchange. The effect of the active bond is only seen in the symmetric part of the mass, $\hat{\rho}_{ij}^e$. Other than these two specific cases, the active bond will do positive or negative work. When $W_F > 0$, the active bond will absorb energy from the active metamaterial. On the other hand, when $W_F < 0$, the active bond will pump energy into the active metamaterial. The total energy absorbed or pumped is proportional to $\hat{\rho}_{12}^o \bar{v}_1 \bar{v}_2$ and in

a sine relationship with the phase difference $\Delta\phi = \phi_1 - \phi_2$ between \dot{u}_1 and \dot{u}_2 (Fig. 1D). In addition, the phases ϕ_1 and ϕ_2 can be viewed as the phase of the excitation active force F_i^o and that of the velocity response \dot{u}_j , respectively. So, the odd mass system behaves like a damped or undamped system depending on $\Delta\phi$. Note that the energy transfer happens under specific conditions, such that phase transitions and exceptional points are foreseen. In this sense, the active metamaterial now becomes a classical Non-Hermitian system with energy loss and gain.

Physical Realization. To realize odd mass density tensors, we propose a design of an active elastic metamaterial with inner resonators by cutting slots from a single-phase plate to form horizontal and vertical beams, which connect the central block and its outer surrounding matrix (see the gray region in Fig. 2A). The central block functions as the inner mass m , and the beams serve as the springs k_1 and k_2 along the \mathbf{x}_1 and \mathbf{x}_2 directions. k_1 and k_2 can be controlled by the thickness and length of those beams. Two piezoelectric patches are bonded on the horizontal beams as stretch sensors, and the sensing signal is fed into a transfer function H that sends to two piezoelectric patches bonded on the vertical beams as actuators (Fig. 2A). When the central block moves vertically, one of the sensing piezoelectric patches is under tension (or compression), and the other is under compression (or tension) (Fig. 2B). The total sensing signal is then obtained from the two opposite charges Q_s from the sensing patches. The transfer function $H(\omega)$ processes the sensing voltage and sends output signals V_a to the two actuating patches, with $V_a = H Q_s / C_0$, where C_0 is the reference capacitance. The two actuating patches with opposite polarizations bend the two vertical beams to produce horizontal forces applied on the central block and the surrounding material, $F_a \propto V_a$ (Fig. 2C). However, when the central block moves horizontally, all the vertical beams are bent and horizontal beams remain nearly straight, as horizontal beams are much stiffer than the vertical ones in response to horizontal motions. As a result, the two sensing patches do not sense the motion and the electronic loop will not produce any output voltages. Therefore, the electromechanical control loop is entirely feed-forward: Vertical motion induces horizontal forces, while horizontal motion does not induce vertical forces.

The design is validated first by performing numerical simulations to calculate the effective mass density tensor of the active metamaterial using COMSOL Multiphysics (Fig. 2D). In the simulations, we prescribe an acceleration, a_i , on the boundaries of the unit cell and calculate the total reactor forces, \bar{F}_i . The effective

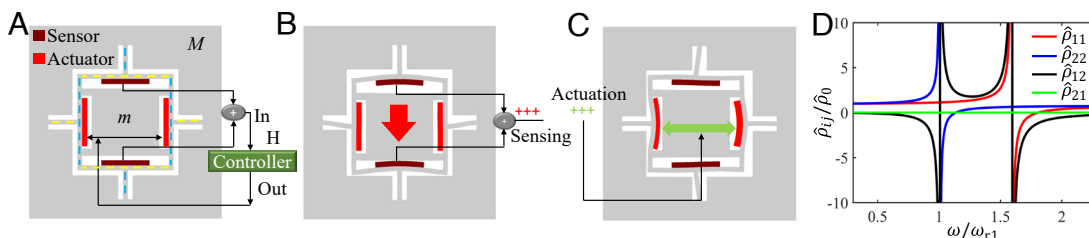


Fig. 2. Active unit cell design for odd mass density. (A) The metamaterial unit cell, which exhibits odd mass, consists of a structured steel frame and four piezoelectric patches (PZT-5A) with two of them being stretch sensors and the other being actuators. The asymmetric actuation is achieved by a programmable controller which connects the sensors (dark red) and actuators (light red) and is characterized by a transfer function H . The inner and outer masses, m and M , are indicated. (B and C) The schematic illustration of deformation distribution reveals how the two orthogonal motions are coupled in a nonsymmetric way: The sensors sense the vertical deformation and feed the sensing voltage processed by the controller to the actuators for horizontal actuation. However, the reverse is forbidden owing to the absence of a horizontal sensor. (D) Numerically obtained effective mass density tensor $\hat{\rho}_{ij}$, normalized with $\hat{\rho}_0 = \hat{\rho}_{11}(\omega = 0.3\omega_{r1})$. The frequency is normalized with the first resonance frequency $\omega_{r1} = 2\pi \times 10.81$ kHz.

mass density tensor is attained based on Eq. 3; *SI Appendix*. In the design, $H = 1$, $C_0 = 2 \text{ nF}$, and the lengths of horizontal and vertical beams facing the central block are different, leading to different resonance frequencies of the horizontal and vertical modes. As shown in Fig. 2D, the resonance behavior of $\hat{\rho}_{11}$ and $\hat{\rho}_{22}$ agrees well with that predicted by Eq. 4. Further, $\hat{\rho}_{12}$ is nonzero and displays a double resonance behavior and $\hat{\rho}_{21}$ indeed vanishes. Therefore, the effective mass density tensor is asymmetric. The design can be employed in further experimental and numerical studies to exploit other profound properties of the odd mass density.

Experiments. We fabricate a unit of the active metamaterial on a steel beam to test its wave transmission properties (Fig. 3A). We also leverage it as a way to show the existence of asymmetric/odd mass density tensors. Details about the fabrication and circuit design as well as implementation can be found in *Materials and Methods* and *SI Appendix*. In the study, we focus on two fundamental modes supported by the beam structures: longitudinal modes dominated by the velocity component u_1

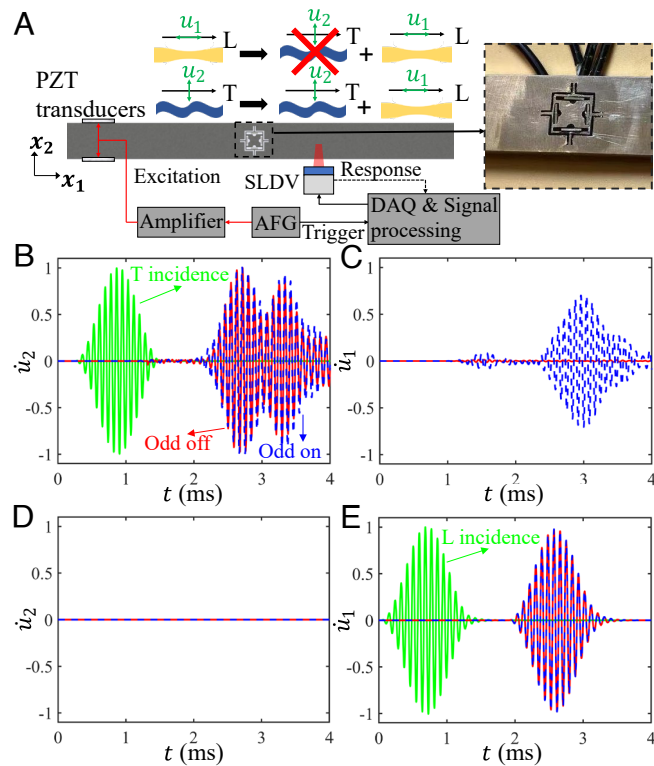


Fig. 3. Experimental demonstration of 1D nonsymmetric wave coupling enabled by odd mass. (A) Schematic of the experimental test bed that includes an active metamaterial with odd mass on a steel host beam. Transverse (T) incidence generates both transverse (T) and longitudinal (L) transmission, whereas the reverse is forbidden. The green arrows define the wave polarization u_1 and u_2 . The inset displays a photo of the metamaterial functional unit. In the experiment, the incidence from the left is excited by two symmetrically placed piezoelectric patches (PZT-5A) connected to an voltage amplifier and arbitrary function generator (AFG); *SI Appendix*. The measurement and postprocessing are implemented by a commercial laser vibrometer system (Polytec PSV-400 3D). (B and C) Measured normalized transient velocities (B) u_2 and (C) u_1 at the output under a transverse incidence when the active control is OFF (red solid) and ON (blue dashed). (D and E) Numerical normalized transient velocities (D) u_2 and (E) u_1 at the output under a longitudinal incidence when the active control is OFF (red solid) and ON (blue dashed). The excitation in both cases is a 15-cycle tone burst centered at 11.3 kHz. The displayed curves are obtained after taking averages on the measured data. The velocities are normalized with the maximums of their own incidence (green).

and transverse modes dominated by the velocity component u_2 . When the beam is symmetric about the neutral axis, the two modes are decoupled. Introducing geometric asymmetry can make the two modes coupled, and the wave mode conversion has been observed in various passive designs (15, 39). However, wave mode interactions demonstrated so far have always been reciprocal, namely longitudinal modes can be converted into transverse modes either partially or totally; transverse modes can also be converted back into longitudinal modes in a similar manner.

The wave mode conversion embraced by the odd mass can no longer be reciprocal. To illustrate this behavior, sensing patches are aligned along the x_1 direction and actuating patches along the x_2 direction (Fig. 3A). Since only transverse motions can be sensed in this case, which in turn generates longitudinal forces thanks to the active bond, transverse waves induce longitudinal waves when passing through the active metamaterial. The wave signals of u_2 and u_1 shown in Fig. 3 B and C demonstrate this behavior, where transmitted waves from the active metamaterial have both u_1 and u_2 components when the control is ON. The u_2 responses with and without the control remain alike, due to the fact that the extraction of the sensed charge in the presence of control does not cause any transverse scattering other than those caused by the structures of sensors and actuators. The active actuation by the control loop and the actuators is always antisymmetric with respect to the transverse motion. In other words, the actuation mainly affects the longitudinal component and only has a very minor influence on the transverse component due to the Poisson's ratio. The experimental results yield satisfactory agreement with numerical simulations (*SI Appendix* and *Movies S1–S4*). On the other hand, no transverse wave components can be observed from a longitudinal incidence, as shown in Fig. 3 D and E. Similarly, if one rotates the active metamaterial by 90°, longitudinal waves induce transverse waves, but not the reverse; *SI Appendix*. Further, the transmitted and reflected signals measured from experiments can be employed to retrieve the effective mass tensors of the active metamaterial, where we can assume the unit embedded in the beam as a point scatterer.

Wave Propagation in 2D Elastic Medium with Odd Mass Density Tensors.

To further explore the nonstandard dynamics supported by odd mass density tensors, we study wave propagation in a 2D active metamaterial. Note that in the subsequent examples, we consider the cases of $\hat{\rho}_{12}^o \in \mathbb{R}$. To facilitate the analysis, it is useful to rewrite the asymmetric mass density tensor along principal directions of the symmetric mass density tensor. The transformed mass density tensor reads (*Materials and Methods*)

$$\tilde{\rho}_{ij} = \begin{bmatrix} \tilde{\rho}_{11} & \tilde{\rho}_{12} \\ -\tilde{\rho}_{12} & \tilde{\rho}_{22} \end{bmatrix}, \quad [9]$$

where $\tilde{\rho}_{ij} = \hat{\rho}_{kl}\tilde{\beta}_{ki}\tilde{\beta}_{lj}$, and $\tilde{\beta}_{ki}$ is the rotation matrix from x_i to \tilde{x}_i with \tilde{x}_i being the principal axis of $\hat{\rho}_{ij}^e$. At continuum limit, equilibrium equations can be written in \tilde{x}_i as

$$(\lambda + \mu) \tilde{u}_{j,ji} + \mu \tilde{u}_{i,jj} = -\omega^2 \tilde{\rho}_{ij} \tilde{u}_j, \quad [10]$$

where \tilde{u}_i , λ , and μ denote the transformed displacement, first, and second Lamé's constants, respectively. We assume harmonic wave solutions $\tilde{u}_\alpha = \tilde{U}_\alpha e^{i(\tilde{q}_\beta \tilde{x}_\beta - \omega t)}$ for Eq. 10, where $\tilde{q}_\beta = q \tilde{r}_\beta$. q and \tilde{r}_β are the wavenumber and direction cosine $\cos \theta_\beta$ where θ_β

is the angle between the principal directional and \mathbf{x}_β . Dispersion relations indicated by Eq. 10 then read

$$q^2 = \omega^2 \frac{I_1 \pm \sqrt{I_1^2 - 4I_2(\tilde{\rho}_{11}\tilde{\rho}_{22} + \tilde{\rho}_{12}^2)}}{2I_2}, \quad [11]$$

where $I_1 = D_{22}\tilde{\rho}_{11} + D_{11}\tilde{\rho}_{22}$, $I_2 = D_{11}D_{22} - D_{12}^2$, and $D_{11} = (\lambda + 2\mu)r_1^2 + \mu r_2^2$, $D_{22} = (\lambda + 2\mu)r_2^2 + \mu r_1^2$, $D_{12} = (\lambda + \mu)r_1r_2$. $r_1 = \arccos\theta_1$ and $r_2 = \arccos\theta_2$ are the direction cosines with respect to $\tilde{\mathbf{x}}_1$ and $\tilde{\mathbf{x}}_2$ after the transformation. Clearly, given a real ω , there always exist two independent modes, characterized by the two solutions of q^2 . Note that the odd mass density of the active metamaterial, $\hat{\rho}_{12}$, is involved in three terms in Eq. 11, $\tilde{\rho}_{11}$ and $\tilde{\rho}_{22}$ as well as $\tilde{\rho}_{12}$ to collectively control wave propagation along different directions.

The most striking characteristics of Eq. 11 is the emergence of the term $\tilde{\rho}_{12}^2$ related to q^2 , and q^2 need not be always greater than zero. For example, when $I_1^2 < 4I_2(\tilde{\rho}_{11}\tilde{\rho}_{22} + \tilde{\rho}_{12}^2)$, q becomes a complex number, indicating energy gain or loss when waves travel along certain directions. The fact of q evolution from originally a real number to a complex number underpins a phase transition governed by the odd mass density. To see the phase transition in more detail, we consider wave propagation along one of the principal directions, in which the effective mass density is smallest (*Materials and Methods*). For simplicity, we assume $\hat{\rho}_{11} = \hat{\rho}_{22}$, $\hat{\beta} = \hat{\rho}_{12}/\hat{\rho}_{11}$, and $\tilde{\mathbf{x}}_i$ is obtained by rotating \mathbf{x}_i by $\pi/4$. Fig. 4 A and B show the real and imaginary parts of the two q with different odd mass densities. Fig. 4 C and D show the real and imaginary parts of the corresponding eigenvectors (polarization states of quasipressure and quasishear modes). For zero or small $\hat{\beta}$ leading to $I_1^2 > 4I_2(\tilde{\rho}_{11}\tilde{\rho}_{22} + \tilde{\rho}_{12}^2)$, there exists two different real q , and the corresponding eigenvectors are both real. $\hat{\rho}_{12}$ only induces anisotropy, which, however, is different from passive anisotropic mass densities, where eigenvectors of different modes are orthogonal. For the active metamaterials presented here, the presence of $\tilde{\rho}_{12}$ makes eigenvectors of different modes no longer orthogonal. Since the system in this phase region is energy conserved, we say that this phase is an energy-unbroken phase.

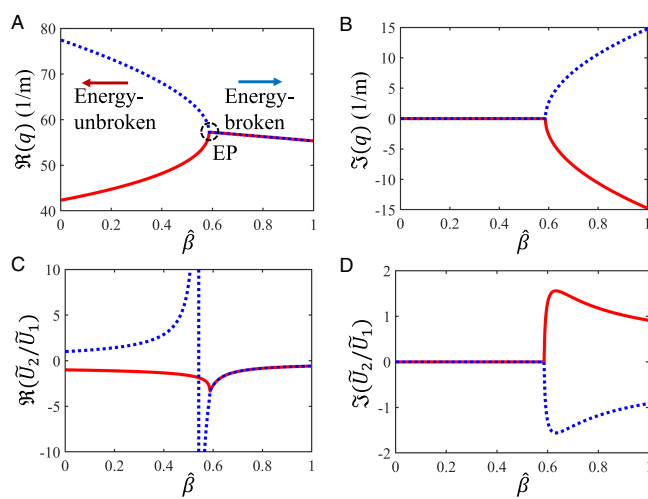


Fig. 4. Energy phase transition at $\theta_1 = 0$ by tuning $\hat{\beta}$. (A) Real and (B) imaginary parts of wave numbers q in function of $\hat{\beta}$. The EP is indicated, together with the energy-unbroken and energy-broken phases. (C) Real and (D) imaginary parts of \tilde{U}_2/\tilde{U}_1 of eigenvectors in function of $\hat{\beta}$. In all figures, we select $\lambda = 37.4$ GPa, $\mu = 27$ GPa, and $\hat{\rho}_{11} = \hat{\rho}_{22} = 16277$ kg/m³.

Further, by increasing $\hat{\beta}$ such that $I_1^2 = 4I_2(\tilde{\rho}_{11}\tilde{\rho}_{22} + \tilde{\rho}_{12}^2)$, the two q and their associated eigenvectors coalesce, forming an exceptional point (EP). Further increasing $\hat{\beta}$ to make $I_1^2 < 4I_2(\tilde{\rho}_{11}\tilde{\rho}_{22} + \tilde{\rho}_{12}^2)$, the two q appear in a complex conjugate pair, and wave propagation accompanied with energy gain (blue mode) and loss (red mode) can be anticipated in this phase region. Thus, we say this phase is an energy-broken phase. In addition to the complex q , the eigenvectors are also complex, coinciding with the work done condition designated by Eq. 8.

Next, we examine the phase transition along different directions. Fig. 5A shows the isofrequency curves for the real part of the wavenumbers, $\Re(q)$, with different odd mass densities. Fig. 5B shows the imaginary part of the wavenumbers, $\Im(q)$, along different directions θ . Note that θ represents the direction angle with respect to \mathbf{x}_1 before transformation. In the figures, we select $\hat{\beta} = 0, 0.4, 0.5865$, and 0.7 . When $\hat{\beta} = 0$, the active metamaterial is reduced to a passive one with isotropic mass densities, where waves travel equally to different directions. In Fig. 5A, blue dashed and red solid curves represent pressure and shear wave modes, respectively. When $\hat{\beta} = 0.4$, no gain and loss can be found along any directions, the active metamaterial is in the energy-unbroken phase. Due to anisotropy, waves propagate at different phase velocities along different directions. In particular, along the principal directions of $\pi/4$, quasipressure waves travel at the higher phase velocities, while quasishear waves travel at the lower phase velocities. Similar conclusions can be attained along the directions of $3\pi/4$, where the principal mass density along this principal direction is largest. When $\hat{\beta} = 0.5865$, two exceptional points are formed along the principal direction with the smallest principal mass density, namely the directions of $\pi/4$ and $5\pi/4$. Further increasing $\hat{\beta}$ to 0.7 , the active metamaterial enters the energy-broken phase around these directions. As expected, $\Im(q)$ becomes nonzero, and waves are attenuated and amplified along those directions. In addition, four exceptional points are formed at the boundaries of those directions. Note also that, for all the cases, the wave behavior obeys mirror symmetry with respect to the principal axes of the even mass density tensor. This is the direct consequence of the q^2 term in Eq. 11. The conclusion that the exceptional points (wave attenuation and amplification) are first observed along the principal direction with the smallest principal mass density still holds when $\hat{\rho}_{11} \neq \hat{\rho}_{22}$. The launch pattern of the exceptional points in the active solid provides a tool to tailor the wave amplification direction using $\hat{\rho}_{11}$ and $\hat{\rho}_{22}$ through designing passive metamaterial structures and a numerical demonstration will be given in the following.

To further examine the energy phase transition and directional wave amplification, harmonic wave propagation in a 2D active medium is conducted by applying cylindrical wave excitation via a point source in COMSOL Multiphysics, as shown in Fig. 6. For simplicity, the active unit is assumed to be the one given in Fig. 2A but preserves C4 structure symmetry to ensure $\hat{\rho}_{11} = \hat{\rho}_{22}$ (*SI Appendix*). The effective odd mass density tensor is determined using Eq. 3, and the effective stiffness tensor is determined numerically by applying macroscopic strain fields (40, 41); see *SI Appendix*, and *Materials and Methods*. To suppress reflected waves from the finite boundaries, the active solid is embedded in a homogenized medium with almost the same effective stiffness tensor attached to the perfectly matched layers (PMLs). From Fig. 6 A and B showing both the divergence and curl of the displacement fields, it can be concluded that the active solid can operate from the energy-unbroken phase to the energy-broken phase through the exceptional points by

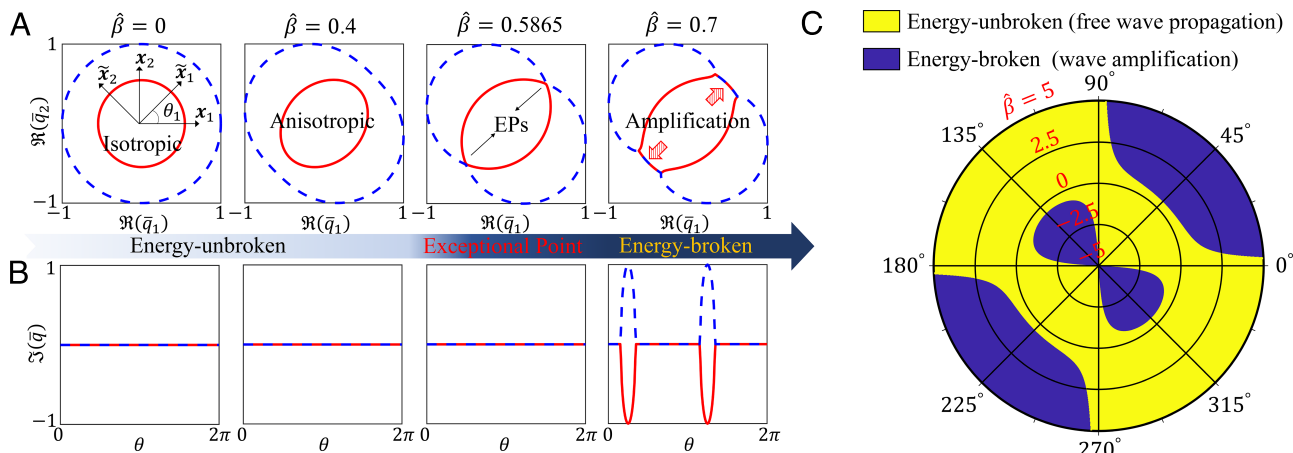


Fig. 5. Energy phase transition. (A) Isofrequency contours $\Re(\tilde{q}_1)$ and $\Re(\tilde{q}_2)$ for both propagating modes when the system operates in energy-unbroken phases (isotropic with $\hat{\beta} = 0$ and anisotropic with $\hat{\beta} = 0.4$), at exceptional point ($\hat{\beta} = 0.5865$), and in energy-broken phase ($\hat{\beta} = 0.7$). \tilde{q} is the wavenumber normalized with the maximum in each case. Principal directions \tilde{x}_1 and \tilde{x}_2 are illustrated by rotating x_1 and x_2 by $\tilde{\theta}_1$. Here, $\tilde{\theta}_1 = \pi/4$ (B) θ dependence of the imaginary components of wave numbers, $\Im(\tilde{q}_1)$ and $\Im(\tilde{q}_2)$, for both modes correspondingly in the four representative phases mentioned in (A). In both (A) and (B), the blue and red modes correspond to those given in Fig. 4. (C) The energy phase diagram in the space of θ in black (azimuthal) and $\hat{\beta}$ in red (radial). The yellow region is the energy-unbroken phase and supports free wave propagation. While the dark blue regions are energy-broken phase where wave amplification occurs.

increasing or decreasing $\hat{\beta}$ from $\hat{\beta} = 0$ (energy conservation). The wave propagation behavior becomes more anisotropic with the increase or decrease of the $\hat{\beta}$ in the energy-unbroken phase. It also indicates strong directional wave amplification when $\hat{\beta} = 1.18$ at which the system operates in the energy-unbroken phase. The directions of the wave amplification indeed coincide with the principal directions of the mass density tensors, which are $\theta_1 = \frac{\pi}{4}/\frac{3\pi}{4}$ and $\frac{5\pi}{4}/\frac{7\pi}{4}$ for $\hat{\beta} = 1.18/-1.18$. Note that minor unexpected scattering at the corners is found in the curl fields for the energy-unbroken phase (Fig. 6B). This is due to the unit cell size being comparable to the operating wavelength, thereby weakening the long-wavelength assumption to some extent. To validate the simulation and related wave phenomena,

comparison of the wave field distributions obtained from both effective medium and real structures at all $\hat{\beta}$ is conducted in *SI Appendix*, and very good agreement is observed. It is also interesting to point out that the wave amplification along the principal directions still holds when the transfer function is a purely imaginary number, say $H = i$, equivalent to $\hat{\beta} = 1.18i$ (*SI Appendix*). In comparison with the cases of real $\hat{\beta}$, here, the wave amplification direction for one of the two modes shifts to the other principal direction by $\pi/2$. It should also be mentioned that the active solid with purely imaginary $\hat{\beta}$ always operates in the energy-broken phase without energy phase transition behavior. It should be noted that since the modulus of the active metamaterial with odd mass density is isotropic in the continuum limit, the

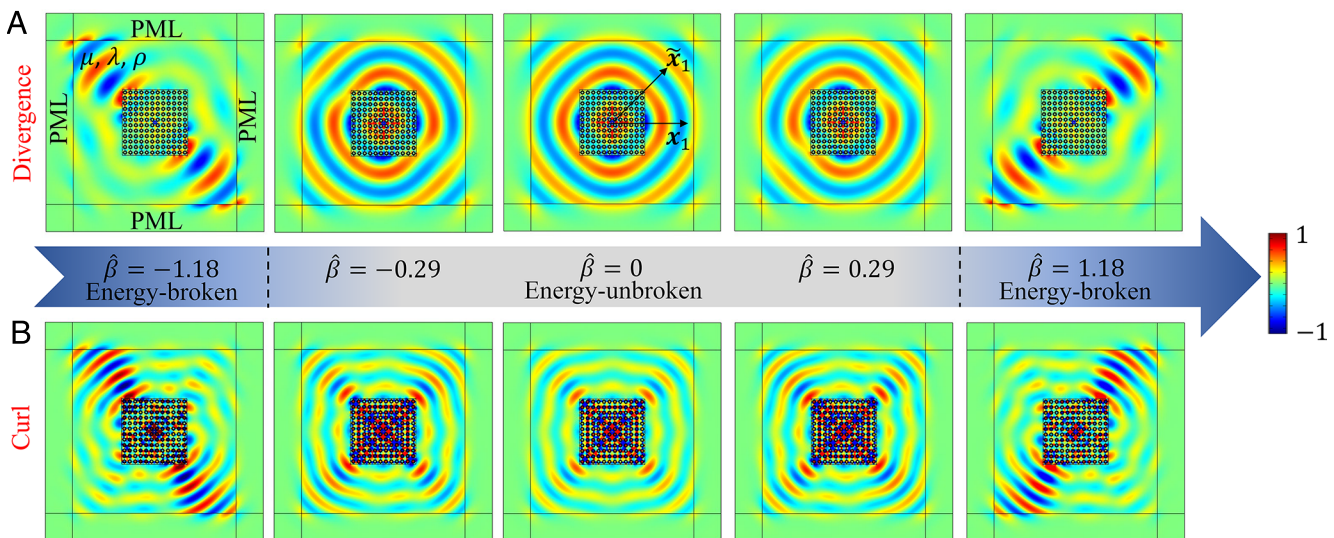


Fig. 6. Numerical demonstration of energy phase transition and directional wave amplification. (A) Numerically evaluated divergence fields of displacement at 16 kHz for various $\hat{\beta}$ under a pressure loading. (B) Numerically evaluated curl fields of displacement at 16 kHz for various $\hat{\beta}$ under a shear loading. In both figures, $\hat{\beta} = 0$ (energy-unbroken isotropic), $\hat{\beta} = \pm 0.29$ (energy-unbroken anisotropic), and $\hat{\beta} = \pm 1.18$ (energy-broken) are achieved with the transfer functions $H = 0$, $H = \pm 0.2$, and $H = \pm 1$, respectively. The 2D odd mass region, composed of 12×12 unit cell and possessing odd mass density (*Materials and Methods* and *SI Appendix*), is embedded in a normal isotropic background ($\rho = 16277 \text{ kg/m}^3$, $\mu = 27.4 \text{ GPa}$, $\lambda = 37 \text{ GPa}$) surrounded with perfect matched layers (PMLs). The point sources for the pressure and shear excitation are realized by setting normal and tangential boundary loads, respectively. The fields obtained from simulations are all normalized with their own maximums. The principal direction \tilde{x}_1 is indicated.

2D stiffness tensor should have the same form as the 1D system when $\hat{\theta} = 0$ or $\pi/2$. Consequently, 2D wave behaviors along the x_1 - or x_2 -directions will resemble those in 1D systems, i.e., nonsymmetric wave coupling (Fig. 3), when a pressure or shear source loading is excited only along the x_1 - or x_2 -directions.

To experimentally demonstrate the 2D directional wave amplification caused by odd mass density, we fabricated an active metamaterial consisting of 2×2 unit cells in a stainless-steel plate (*Materials and Methods* and *SI Appendix*). The odd mass density is physically realized with the help of connected analog circuits (*SI Appendix*). The experimental setup of measuring wave propagation is shown in Fig. 7A and detailed in *Materials and Methods*. Two piezoelectric patches at the center of the metamaterial region are symmetrically bonded on the two surfaces of the plate as actuators to generate cylindrical pressure waves. Then, we select two scanning regions ($291.2 \times 291.2 \text{ mm}^2$), located symmetrically with respect to the active metamaterial, to demonstrate the directional wave amplification. The time-dependent velocity fields in both x_1 - and x_2 -directions are measured when the external circuits are switched on and off to activate and deactivate the odd mass density. The divergence fields derived from the measured wave fields are displayed in Fig. 7B and C without and with the active control, respectively. As shown in Fig. 7B, when the control is switched off, the metamaterial is purely passive and does not exhibit odd mass density. It is evidenced that the measured wave fields in the two regions are almost symmetric, representing the isotropic scenario ($\hat{\beta} = 0$) depicted in Fig. 6. When the control is activated (Fig. 7C), the appearance of odd mass density results in the amplification of pressure waves propagating within the region I. In contrast, the measured field in the region II resembles that in the passive scenario, and no obvious wave amplification can be observed (*Movies S1–S4*). To demonstrate this behavior quantitatively, the magnitude of the measured divergence field on a predefined curve is plotted in Fig. 7D for both active

and passive scenarios. The difference in magnitude between two configurations clearly evidences the 2D directional amplification for pressure waves around $5\pi/4$, corresponding to the local direction around $\Theta \approx \pi/4$ in Fig. 7D. It should be noticed that the directional wave amplification can be enhanced by increasing the number of active unit cells; *SI Appendix*. Furthermore, the corresponding 2D harmonic simulation under the plane-stress assumption qualitatively verifies the transient experiments (Fig. 7E). The small discrepancy from the experiments is due to the use of a perfect circular source in the numerical simulation, instead of the real piezoelectric actuator. Additionally, *SI Appendix* presents the numerical comparison between the real structure and the corresponding effective homogeneous medium. Satisfactory agreement can be observed, indicating that the 2×2 active array can be effectively treated as a homogeneous metamaterial possessing odd mass density.

Anisotropic mass densities, namely $\hat{\rho}_{11} \neq \hat{\rho}_{22}$, provide another degree of freedom in tuning directions of the wave amplification in the active solid. Due to the anisotropy, the principal directions of the mass density differ from those of the isotropic mass density with different phase velocities. In this way, the wave amplification directions can be adjusted accordingly. To illustrate this wave phenomenon, the normalized divergence and curl fields of wave displacement are plotted in Fig. 8 for the effective active media with $\hat{\rho}_{22}/\hat{\rho}_{11} = 0.1$ and 2, and $\hat{\beta}$ fixed at 0.6144. The angle change of directional wave amplification for both pressure and shear waves confirms the functionality of the mass density anisotropy. The predicted angles of directional wave amplification are indeed mainly along the principal directions of the mass density from the analytical analysis (*Materials and Methods*). Some discrepancies are observed, which may attribute to the material impedance mismatch between the real active solid and its surrounding background. In addition, the complete angle $\tilde{\theta}_1$ tunability of directional wave amplification due to the mass density anisotropy is systematically investigated when

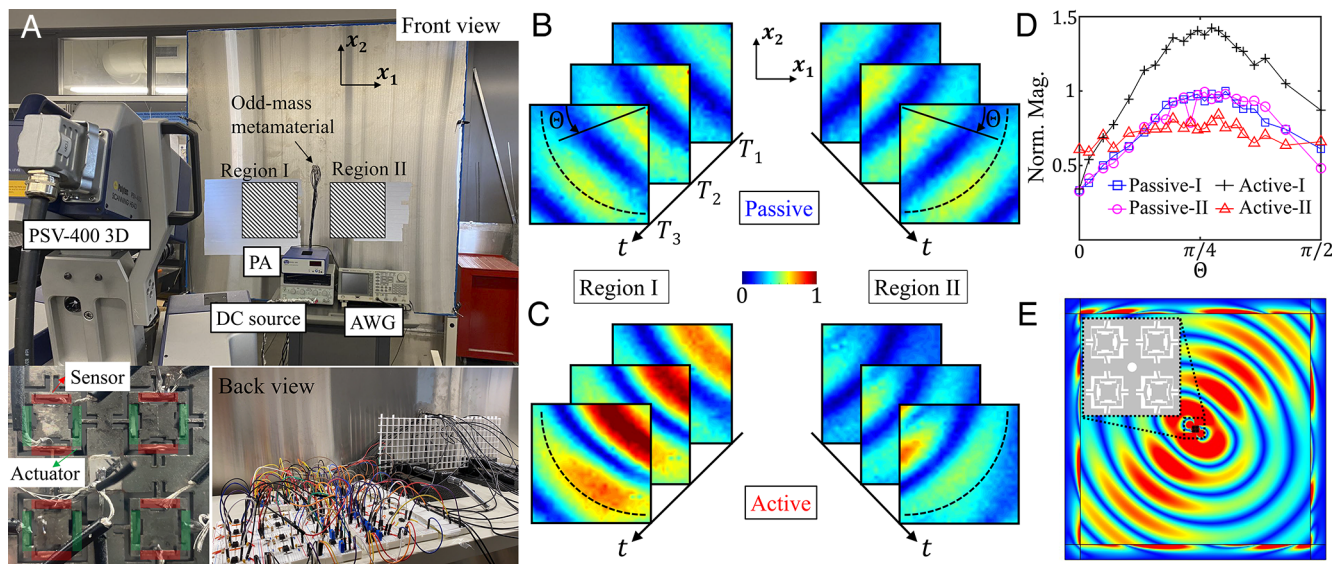


Fig. 7. Experimental demonstration of 2D directional wave amplification. (A) Experimental setup for the demonstration of the 2D directional pressure wave amplification induced by odd mass density at 14 kHz. The odd-mass region and the back view are displayed on the bottom. (B and C) Snapshots of the divergence of the measured velocity fields within the scanning regions with (B) and without (C) the active control. Three representative time instants are selected as $T_1 = 0.068 \text{ ms}$, $T_2 = 0.088 \text{ ms}$, and $T_3 = 0.126 \text{ ms}$. A predefined dashed curve for the evaluation of wave amplification is assigned, with Θ being the local scan angle. (D) Dependence of field magnitude on the local angle Θ for all the cases included in (B and C). Magnitudes are collected at T_3 on the predefined dashed curves and normalized with respect to the maximum in the case of Passive-I. (E) Numerically obtained divergence field magnitude distribution at 14 kHz. The simulation domain is surrounded by perfect matched layers. All the geometrical, material, and electrical parameters are identical to those used in the experiments. The inset highlights the deformation pattern of the active unit cells upon cylindrical pressure loading.

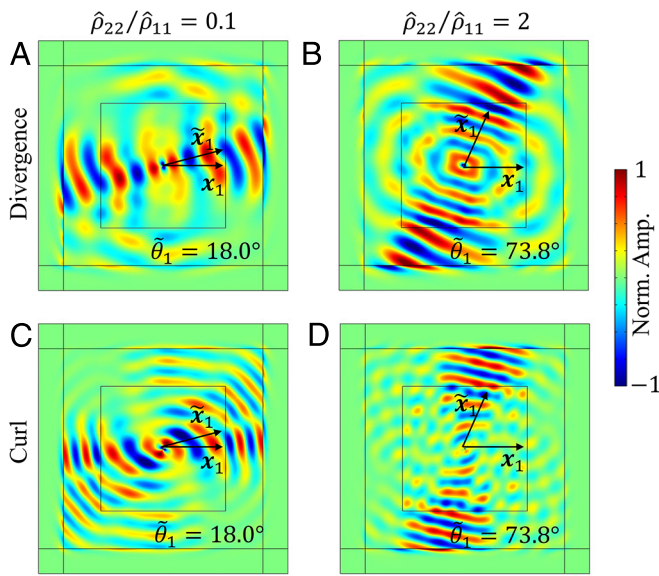


Fig. 8. Wave manipulation with anisotropic odd mass density tensor. (A and B) Normalized divergence fields of displacement at (A) $\hat{\rho}_{22}/\hat{\rho}_{11} = 0.1$ and (B) $\hat{\rho}_{22}/\hat{\rho}_{11} = 2$. (C and D) Normalized curl fields of displacement at (C) $\hat{\rho}_{22}/\hat{\rho}_{11} = 0.1$ and (D) $\hat{\rho}_{22}/\hat{\rho}_{11} = 2$. $\hat{\beta} = 0.6144$ is assumed (energy-broken phase). The background media are the same as the previous. The stiffness property of the odd mass regions ($500 \text{ mm} \times 500 \text{ mm}$) is consistent with that of the background in order to improve impedance matching. In both field plots, $\hat{\rho}_{11}$ is selected as $16,277 \text{ kg/m}^3$. The field intensities are normalized with their own maximums at 16 kHz. On the bottom of each field plot, the theoretical principal direction $\tilde{\theta}_1$, defining x_1 and predicting maximum amplification steering angle, is indicated in red.

$\hat{\rho}_{22}/\hat{\rho}_{11}$ takes values between 0.1 and 2, which is illustrated in *SI Appendix*.

Non-Hermitian Skin Effect. As the active solid with odd mass density is a non-Hermitian system, it is also interesting to find how the non-Hermiticity would influence the nature of bulk modes. To start with, we impose open boundary condition (OBC) and periodic boundary condition (PBC) along x_2 direction in the finite active solid and assume $q_1 = 1 \text{ rad/m}$ in reciprocal space along the x_1 direction. The spectra for $\hat{\beta} = 0.2$ and $\hat{\beta} = 0.9$ are plotted in Fig. 9 A and B, respectively. We find that the OBC and PBC spectra coincide in the energy-unbroken region with $\hat{\beta} = 0.2$ but are drastically distinct from each other in the energy-broken region with $\hat{\beta} = 0.9$. To retrace this spectral discrepancy, the vertical wave number q_2 should be extended on the generalized Brillouin zone (GBZ), which is a loop on the complex plane, *SI Appendix* for the derivation of the GBZ (42). Fig. 9 C and D illustrate the eigenmodes under OBC for $\hat{\beta} = 0.2$ and $\hat{\beta} = 0.9$, respectively. The active solids can only host bulk modes when the system is in the energy-unbroken phase (43, 44). However, we notice that some eigenmodes localize to the open edges when the system is in an energy-broken phase, which corresponds to an elastic manifestation of the non-Hermitian skin effect (28, 45, 46). The complex frequency means that the skin modes are amplified (attenuated) for positive (negative) $\Im(\text{frequency})$. This skin mode is different from the Rayleigh wave mode whose amplitude is invariant since the frequency is real in classic elasticity. In addition, the skin modes always appear in pairs with one localized on the *Top* while the other on the *Bottom* since the eigenfrequencies always exhibit complex conjugate in the energy-broken phase (*SI Appendix*).

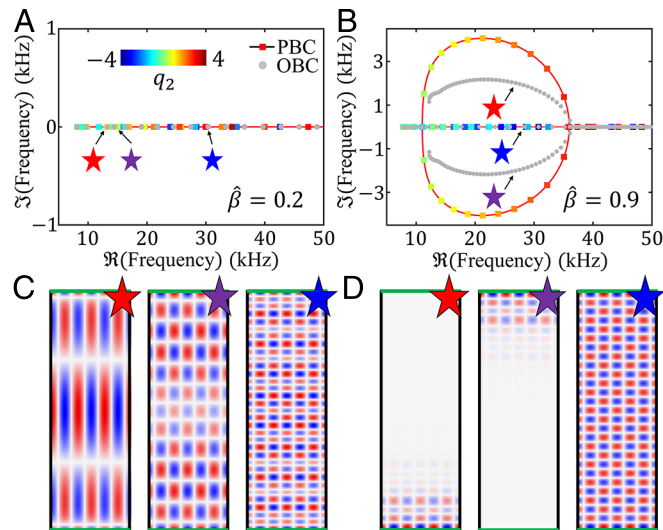


Fig. 9. Non-Hermitian skin effect induced by odd density. (A and B) The complex spectrum when the system operates at $\hat{\beta} = 0.2$ and 0.9. The squares with the hue indicating the wavenumber q_2 and gray circular scatters are results from PBC and OBC, respectively. (C) Numerically computed OBC eigenmodes at $\hat{\beta} = 0.2$ for a finite ribbon. The corresponding eigenfrequencies are 12.94, 15.48, and 30.30 kHz from *Left* to *Right*. (D) Numerically computed eigenmodes at $\hat{\beta} = 0.9$. The corresponding eigenfrequencies are $27.71 + 0.324i$, $27.71 - 0.324i$, and 28.14 kHz from *Left* to *Right*. The *Top* and *Bottom* are set with open boundary conditions. Without loss of generality, the horizontal wave number is fixed at $q_1 = 1 \text{ rad/m}$.

Conclusion

In conclusion, the active metamaterial presented here demonstrates odd mass density that is enabled by sensing, actuating, and local computation. The minimal on-board electronics that power the interior local resonators enable its non-Hermitian wave functions including the directional wave amplification and the non-Hermitian skin effect. Odd mass density extends the range of possible couplings between conventional forces and deformation along two perpendicular directions by including antisymmetry in their relationship. Our design can be flexibly tuned through computer coding and scaled via microelectromechanical systems (MEMS). The mechanical approach relies on a feed-forward control loop, a generic concept that can exist in both metamaterial and biological contexts. It should be emphasized that the active system also possesses a generalized PT symmetry to admit the pseudo-Hermiticity (*Materials and Methods*), stating $[\mathcal{K}, \hat{\rho}_{ij}^{-1} D] = 0$, where \mathcal{K} is an antiunitary complex conjugation operator (28). Combining the principles illustrated here with odd moduli, nonlinearities, and strong dissipation suggests different approaches for the control of wave propagation in active solids and fluids.

Materials and Methods

Sample Fabrication. The odd-mass metamaterial beam in the 1D experiments is constructed by mounting four piezoelectric patches (APC PZT-5A, $5 \times 0.55 \times 0.55 \text{ mm}^3$) via conductive epoxy onto a laser-cut stainless steel host beam. The two actuating piezoelectric patches are oppositely polarized such that the two vertical beams are bent producing forces applied on the central block and the surrounding material. In the 2D experiments, four odd-mass unit cells are manufactured using a laser cutting technique in a stainless steel host plate ($1,700 \times 1,700 \times 3 \text{ mm}^3$). To suppress the reflection from plate boundaries, the plate is wrapped with a layer of damping clay. Sixteen piezoelectric patches (APC PZT5-A, $6 \times 3 \times 0.72 \text{ mm}^3$) are mounted via a conductive epoxy (CW 2400)

onto the cutting area to serve as sensors and actuators for the four unit cells. The sensors and actuators are connected by a homemade analog circuit consisting of charge amplifiers, low-pass filters, and voltage amplifiers (*SI Appendix*). The circuit works as a transfer function for input and output signals, which reads

$$H(\omega) = \frac{H_0}{-\omega^2/\omega_c^2 + 2i\eta\omega/\omega_c + 1}, \quad [12]$$

where $H_0 = 30$, $\omega_c = 2\pi \times 33.5$ kHz and $\eta = 0.4$. Adopting this transfer function enforces the system stability.

Experimental Protocols. In the 1D experiments, an odd mass metamaterial unit cell is connected with external control circuits, see the schematics in Fig. 3 and *SI Appendix*. Two piezoelectric transducers are attached on the *Top* and *Bottom* sides of the host beam to generate transverse incidence. The transfer function used reads $H(\omega) = H_0/(\omega^2/\omega_0^2 + 2\xi\omega/\omega_0 + 1)$, where $H_0 = 2 \times 10^8$, $\xi = 0.5$ and $\omega_0 = 2\pi \times 15$ kHz. We employ fifteen-cycle tone-burst signals with a central frequency of 11.3 kHz. We generate and amplify incident wave signals via an arbitrary waveform generator (Tektronix AFG3022C) and a high-voltage amplifier (Krohn-Hite), respectively. In-plane velocity wave fields for u and v are measured on the surface of the right side of the metamaterial by a scanning laser Doppler vibrometer (Polytec PSV-400). To suppress reflected waves at the boundaries of the host beam, we clamp the edge and bond two layers of clay on the host beam with sufficient lengths. This way, waves can propagate through the metamaterial with approximated infinite boundary conditions in the background (47). The time-domain signals shown in Fig. 3 are collected 120 mm away from the right boundary of the odd-mass metamaterial. In the experimental measurement, a ten-cycle tone-burst voltage signal $V(t) = V_0 \sin(2\pi f_ct) [1 - \cos(2\pi f_ct/10)]$ with a central frequency $f_c = 14$ kHz and $V_0 = 500$ V is employed on the central piezoelectric actuators to generate cylindrical pressure waves. The excitation signal is first produced by the arbitrary waveform generator (Tektronix AFG3022C) and then amplified by a high-voltage amplifier (Trek Model 2205). Reflective tapes were used to enhance the reflected signals of the laser beams from the sample. In-plane velocity fields are measured using the 3D scanning laser Doppler vibrometer (Polytec PSV-400 3D). Then, 33×33 scan points are assigned within the 291.2×291.2 mm² scanning area to obtain satisfactory resolutions. In order to suppress background noise and improve the signal-to-noise ratio, a band-pass filter covering 12 to 20 kHz is implemented during the postprocessing, and the collected time-domain data are averaged ten times during the measurement.

Finite Element Simulations. We use COMSOL Multiphysics to determine the homogenized properties of the odd-mass unit cell and obtain the 2D field distributions for both real structures and homogenized media. In all the simulations, we model the piezoelectric patches via a 3D linear piezoelectric constitutive law. The top and bottom piezoelectric patches act as sensors whose signals are obtained by integrating the free charge over the top surfaces of the sensors. Also, the top and bottom surfaces of the sensors have vanishing electric potential. The bottom surfaces of the piezoelectric actuators are grounded, and we apply electrical potentials, acting as actuating voltages, on their top surfaces. The actuating voltages are determined based on the sensing voltages via the electronic transfer function H . For the frequency-domain simulations in Fig. 3, free boundary conditions are applied on the top and bottom boundaries of the beam. Two perfect matched layers (PML) are placed on the left and right edges of the beam in order to suppress reflected waves from the boundaries. The incidence is generated by applying a harmonic force on the left of the odd-mass metamaterial. To simulate the wave propagation given in Fig. 6, a metamaterial composed of 12×12 odd mass unit cells is placed within a normal isotropic medium. PMLs are then attached to surround the background ensuring the suppression of reflected waves. The point source at the center is constructed as a small circle. The cylindrical pressure and shear excitation are generated by applying boundary-normal and boundary-tangential harmonic forces on the small circle, respectively. In the simulations for homogenized models, we replace the 12×12 metamaterial with a homogenized square with the same overall size.

The effective odd mass density tensor and the orthotropic elasticity tensor by homogenization are entered using weak-form formulations.

Principal Direction of Odd Mass Density Tensor. Based upon Eq. 7, we can separate the odd mass density tensor into even and odd parts. The principal mass density and directions can be found by solving eigenvalue problem for the even part

$$\hat{\rho}_{ij}^e = \begin{bmatrix} \hat{\rho}_{11} & \hat{\rho}_{12}^e \\ \hat{\rho}_{21} & \hat{\rho}_{22} \end{bmatrix}. \quad [13]$$

The eigenvalues read

$$\lambda_{1,2} \equiv \tilde{\rho}_{11,22} = \frac{\hat{\rho}_{11} + \hat{\rho}_{22} \pm \sqrt{(\hat{\rho}_{11} - \hat{\rho}_{22})^2 + 4\hat{\rho}_{12}^e\hat{\rho}_{21}^e}}{2}, \quad [14]$$

with $\hat{\rho}_{12}^e = \hat{\rho}_{21}^e = \hat{\rho}_{12}/2$. The corresponding eigenvectors can be written as a transformation matrix $\tilde{\beta}$ reading

$$\tilde{\beta} = \begin{bmatrix} \cos \tilde{\theta}_1 & -\sin \tilde{\theta}_1 \\ \sin \tilde{\theta}_1 & \cos \tilde{\theta}_1 \end{bmatrix}, \quad [15]$$

where the principal orientation of the smallest mass density takes $\tan(2\tilde{\theta}_1) = 2\hat{\rho}_{12}^e/(\hat{\rho}_{22} - \hat{\rho}_{11})$, since

$$(\hat{\rho}_{22} - \hat{\rho}_{11}) \cos \tilde{\theta}_1 \sin \tilde{\theta}_1 = \hat{\rho}_{12}^e (\cos^2 \tilde{\theta}_1 - \sin^2 \tilde{\theta}_1), \quad [16]$$

must hold. While the odd part $\hat{\rho}_{ij}^o$ given in Eq. 7 is invariant under the transformation, namely

$$\hat{\rho}_{kl}^o \tilde{\beta}_{ki} \tilde{\beta}_{lj} = \hat{\rho}_{ij}^o = \begin{bmatrix} 0 & \hat{\rho}_{12}^o \\ -\hat{\rho}_{12}^o & 0 \end{bmatrix}, \quad [17]$$

with $\hat{\rho}_{12}^o = \hat{\rho}_{12}/2$. In this sense, the transformed mass density tensor reads

$$\tilde{\rho}_{ij} = \hat{\rho}_{kl} \tilde{\beta}_{ki} \tilde{\beta}_{lj} = \hat{\rho}_{kl}^e \tilde{\beta}_{ki} \tilde{\beta}_{lj} + \hat{\rho}_{ij}^o = \begin{bmatrix} \tilde{\rho}_{11} & \hat{\rho}_{12}^o \\ -\hat{\rho}_{12}^o & \tilde{\rho}_{22} \end{bmatrix}, \quad [18]$$

which represents Eq. 9.

Pseudo-Hermiticity. We clarify that the system with odd mass density is η -pseudo-Hermitian and exhibits a generalized PT symmetry. Based on ref. (46), a 2×2 matrix \mathbf{Q} with pseudo-Hermiticity can be written as

$$\mathbf{Q} = \epsilon \sigma_0 + (\gamma \mathbf{n}_1 + i\xi \sin \alpha \mathbf{n}_2 + i\xi \cos \alpha \mathbf{n}_3) \cdot \boldsymbol{\sigma}, \quad [19]$$

where σ_0 is a 2×2 identity matrix and $\boldsymbol{\sigma} = (\sigma_x, \sigma_y, \sigma_z)^T$ are Pauli matrices, with

$$\mathbf{n}_1 = (\sin \Gamma \cos \Phi, \sin \Gamma \sin \Phi, \cos \Gamma), \quad [20]$$

$$\mathbf{n}_2 = (\cos \Gamma \cos \Phi, \cos \Gamma \sin \Phi, -\sin \Gamma), \quad [21]$$

$$\mathbf{n}_3 = (-\sin \Phi, \cos \Phi, 0). \quad [22]$$

The pseudo-Hermitian matrix \mathbf{Q} admits 6 real variables and is said to be $\mathbf{n}_1 \cdot \boldsymbol{\sigma}$ -pseudo-Hermitian. Its eigenvalues read

$$\lambda_{1,2} = \epsilon \pm \sqrt{\gamma^2 - \xi^2}. \quad [23]$$

The spectrum of \mathbf{Q} is real when $\gamma^2 - \xi^2 > 0$. Then, it is always accompanied with a positive definite operator η reading

$$\eta = p[\gamma \sigma_0 + (o \mathbf{n}_1 + \gamma \cos \alpha \mathbf{n}_2 - \gamma \sin \alpha \mathbf{n}_3) \cdot \boldsymbol{\sigma}], \quad [24]$$

and resulting in

$$\eta \mathbf{Q} \eta^{-1} = \mathbf{Q}^\dagger. \quad [25]$$

Above, p and o are arbitrary real constants satisfying the conditions $p\gamma > 0$ and $o^2 < \gamma^2 - \xi^2$. In our case, we have

$$\mathbf{D}\mathbf{u} = -\omega^2 \hat{\mathbf{M}}\mathbf{u}. \quad [26]$$

The above is written as

$$\begin{bmatrix} (\lambda + 2\mu)c^2 + \mu s^2 & (\lambda + \mu)cs \\ (\lambda + \mu)cs & (\lambda + 2\mu)s^2 + \mu c^2 \end{bmatrix} \mathbf{u} = \frac{\omega^2}{q^2} \begin{bmatrix} \hat{\rho}_{11} & \hat{\rho}_{12} \\ 0 & \hat{\rho}_{22} \end{bmatrix} \mathbf{u}, \quad [27]$$

in which $c \equiv \cos \theta$ and $s \equiv \sin \theta$. Without loss of generality, we select $\hat{\rho}_{11} = \hat{\rho}_{22} = \hat{\rho}_c$ and $\hat{\rho}_{12} = \hat{\beta} \hat{\rho}_c$. By rearranging Eq. 27, we arrive at

$$\begin{bmatrix} A - B\hat{\beta} & B - C\hat{\beta} \\ B & C \end{bmatrix} \mathbf{u} = \frac{\hat{\rho}_c \omega^2}{q^2} \mathbf{u}, \quad [28]$$

where

$$A = (\lambda + 2\mu)c^2 + \mu s^2, \quad [29]$$

$$B = (\lambda + \mu)cs, \quad [30]$$

$$C = (\lambda + 2\mu)s^2 + \mu c^2. \quad [31]$$

Comparing Eq. 28 with Eq. 19, one can easily find that our system can be expressed by Eq. 19 with the substitutions

$$\epsilon = \frac{1}{2}(A + C - \hat{\beta}B), \quad [32]$$

$$\gamma = -\frac{1}{2}\hat{\beta}C, \quad [33]$$

$$\rho \cos \Gamma = \frac{1}{2}(A - C - \hat{\beta}B), \quad [34]$$

$$\rho \sin \Gamma = \frac{1}{2}(2B - \hat{\beta}C), \quad [35]$$

1. Z. Liu *et al.*, Locally resonant sonic materials. *Science* **289**, 1734–1736 (2000).
2. M. Kadic, T. Bückmann, R. Schittny, M. Wegener, Metamaterials beyond electromagnetism. *Rep. Progr. Phys.* **76**, 126501 (2013).
3. K. Bertoldi, V. Vitelli, J. Christensen, M. Van Hecke, Flexible mechanical metamaterials. *Nat. Rev. Mater.* **2**, 1–11 (2017).
4. H. Huang, C. Sun, G. Huang, On the negative effective mass density in acoustic metamaterials. *Int. J. Eng. Sci.* **47**, 610–617 (2009).
5. H. Yasuda, J. Yang, Reentrant origami-based metamaterials with negative Poisson's ratio and bistability. *Phys. Rev. Lett.* **114**, 185502 (2015).
6. K. T. Tan, H. Huang, C. Sun, Optimizing the band gap of effective mass negativity in acoustic metamaterials. *Appl. Phys. Lett.* **101**, 241902 (2012).
7. H. Huang, C. Sun, Wave attenuation mechanism in an acoustic metamaterial with negative effective mass density. *New J. Phys.* **11**, 013003 (2009).
8. M. Kadic, T. Bückmann, R. Schittny, P. Gumbsch, M. Wegener, Pentamode metamaterials with independently tailored bulk modulus and mass density. *Phys. Rev. Appl.* **2**, 054007 (2014).
9. H. Zhu, S. Patnaik, T. F. Walsh, B. H. Jared, F. Semperlotti, Nonlocal elastic metasurfaces: Enabling broadband wave control via intentional nonlocality. *Proc. Natl. Acad. Sci. U.S.A.* **117**, 26099–26108 (2020).
10. Z. Wang, Q. Zhang, K. Zhang, G. Hu, Tunable digital metamaterial for broadband vibration isolation at low frequency. *Adv. Mater.* **28**, 9857–9861 (2016).
11. H. Nassar, Y. Chen, G. Huang, Polar metamaterials: A new outlook on resonance for cloaking applications. *Phys. Rev. Lett.* **124**, 084301 (2020).
12. X. Xu *et al.*, Physical realization of elastic cloaking with a polar material. *Phys. Rev. Lett.* **124**, 114301 (2020).
13. T. Bückmann, M. Thiel, M. Kadic, R. Schittny, M. Wegener, An elasto-mechanical unfeelability cloak made of pentamode metamaterials. *Nat. Commun.* **5**, 1–6 (2014).
14. T. Bückmann, M. Kadic, R. Schittny, M. Wegener, Mechanical cloak design by direct lattice transformation. *Proc. Natl. Acad. Sci. U.S.A.* **112**, 4930–4934 (2015).
15. J. M. Kweun, H. J. Lee, J. H. Oh, H. M. Seung, Y. Y. Kim, Transmodal Fabry-Pérot resonance: Theory and realization with elastic metamaterials. *Phys. Rev. Lett.* **118**, 205901 (2017).
16. R. Zhu, X. Liu, G. Hu, C. Sun, G. Huang, Negative refraction of elastic waves at the deep-subwavelength scale in a single-phase metamaterial. *Nat. Commun.* **5**, 1–8 (2014).
17. Y. Lai, Y. Wu, P. Sheng, Z. Q. Zhang, Hybrid elastic solids. *Nat. Mater.* **10**, 620–624 (2011).
18. Y. Wu, Y. Lai, Z. Q. Zhang, Elastic metamaterials with simultaneously negative effective shear modulus and mass density. *Phys. Rev. Lett.* **107**, 105506 (2011).
19. H. Yasuda *et al.*, Origami-based impact mitigation via rarefaction solitary wave creation. *Sci. Adv.* **5**, eaau2835 (2019).
20. T. Frenzel, M. Kadic, M. Wegener, Three-dimensional mechanical metamaterials with a twist. *Science* **358**, 1072–1074 (2017).

$$\Phi = \alpha = 0. \quad [36]$$

Therefore, our odd-mass system admits η_θ -pseudo-Hermiticity, where $\eta_\theta = \mathbf{n}_1(\Gamma) \cdot \boldsymbol{\sigma}$. The condition $\gamma^2 - \rho^2 > 0$ for real spectrum of ω^2 can be recast as

$$\hat{\beta}^2 B^2 - 2B^2(A + C)\hat{\beta} + 4B^2 + (A - C)^2 > 0. \quad [37]$$

Therefore, the PT-unbroken regions, shown in Fig. 5, are determined by

$$\hat{\beta} > \frac{2(A + C)}{B} + \frac{2}{B^2} \sqrt{B^2 AC - B^4}, \quad [38]$$

$$\hat{\beta} < \frac{2(A + C)}{B} - \frac{2}{B^2} \sqrt{B^2 AC - B^4}. \quad [39]$$

By calculation, one can find that the PT-unbroken and PT-broken phase regions coincide with the energy-unbroken and energy-broken regions, respectively.

Data, Materials, and Software Availability. All data needed to evaluate the conclusions in the paper are present in the paper (*SI Appendix* and *Movies S1–S4*). The related codes are uploaded to GitHub: https://github.com/wqdsgsy/Odd_Mass_Density.

ACKNOWLEDGMENTS. This work is supported by the Air Force Office of Scientific Research under Grant No. AF 9550-18-1-0342 and AF 9550-20-0-279 with Program Manager Dr. Byung-Lip (Les) Lee and the Army Research Office under Grant No. W911NF-18-1-0031 with Program Manager Dr. Daniel P. Cole.

Author affiliations: ^aDepartment of Mechanical and Aerospace Engineering, University of Missouri, Columbia, MO 65211; ^bDepartment of Mechanics, Beijing Institute of Technology, Beijing 100081, People's Republic of China; and ^cDepartment of Mechanical and Aerospace Engineering, The Hong Kong University of Science and Technology, Hong Kong, China

21. H. Nassar *et al.*, Nonreciprocity in acoustic and elastic materials. *Nat. Rev. Mater.* **5**, 667–685 (2020).
22. X. Xu *et al.*, Physical observation of a robust acoustic pumping in waveguides with dynamic boundary. *Phys. Rev. Lett.* **125**, 253901 (2020).
23. Q. Wu, H. Chen, H. Nassar, G. Huang, Non-reciprocal Rayleigh wave propagation in space-time modulated surface. *J. Mech. Phys. Solids* **146**, 104196 (2021).
24. M. I. Rosa, M. Ruzzene, Dynamics and topology of non-Hermitian elastic lattices with non-local feedback control interactions. *New J. Phys.* **22**, 053004 (2020).
25. Y. Xia *et al.*, Experimental observation of temporal pumping in electromechanical waveguides. *Phys. Rev. Lett.* **126**, 095501 (2021).
26. L. Sirota, R. Ilan, Y. Shokef, Y. Lahini, Non-Newtonian topological mechanical metamaterials using feedback control. *Phys. Rev. Lett.* **125**, 256802 (2020).
27. C. Scheibner *et al.*, Odd elasticity. *Nat. Phys.* **16**, 475–480 (2020).
28. C. Scheibner, W. T. Irvine, V. Vitelli, Non-Hermitian band topology and skin modes in active elastic media. *Phys. Rev. Lett.* **125**, 118001 (2020).
29. S. Shankar, A. Souslov, M. J. Bowick, M. C. Marchetti, V. Vitelli, Topological active matter. *Nat. Rev. Phys.* **4**, 380–398 (2022).
30. Y. Chen, X. Li, C. Scheibner, V. Vitelli, G. Huang, Realization of active metamaterials with odd micropolar elasticity. *Nat. Commun.* **12**, 1–12 (2021).
31. M. Brandenburger, X. Locsin, E. Lerner, C. Coulais, Non-reciprocal robotic metamaterials. *Nat. Commun.* **10**, 1–8 (2019).
32. A. Ghatak, M. Brandenburger, J. Van Wezel, C. Coulais, Observation of non-Hermitian topology and its bulk-edge correspondence in an active mechanical metamaterial. *Proc. Natl. Acad. Sci. U.S.A.* **117**, 29561–29568 (2020).
33. M. Brandenburger, C. Scheibner, J. Veenstra, V. Vitelli, C. Coulais, Limit cycles turn active matter into robots. arXiv [Preprint] (2022). <https://doi.org/10.48550/arXiv.2108.08837> (Accessed 6 November 2022).
34. M. I. Rosa, M. Mazzotti, M. Ruzzene, Exceptional points and enhanced sensitivity in PT-symmetric continuous elastic media. *J. Mech. Phys. Solids* **149**, 104325 (2021).
35. C. Shi *et al.*, Accessing the exceptional points of parity-time symmetric acoustics. *Nat. Commun.* **7**, 1–5 (2016).
36. Q. Wu, Y. Chen, G. Huang, Asymmetric scattering of flexural waves in a parity-time symmetric metamaterial beam. *J. Acous. Soc. Am.* **146**, 850–862 (2019).
37. X. Zhou, G. Hu, Analytic model of elastic metamaterials with local resonances. *Phys. Rev. B* **79**, 195109 (2009).
38. X. Zhou, X. Liu, G. Hu, Elastic metamaterials with local resonances: An overview. *Theor. Appl. Mech. Lett.* **2**, 041001 (2012).
39. Q. Wu, G. Huang, Omnidirectional wave polarization manipulation in isotropic polar solids. *Int. J. Solids Struct.* **241**, 111481 (2022).
40. X. Liu, G. Hu, C. Sun, G. Huang, Wave propagation characterization and design of two-dimensional elastic chiral metacomposite. *J. Sound Vib.* **330**, 2536–2553 (2011).
41. Y. Wu, Y. Lai, Z. Q. Zhang, Effective medium theory for elastic metamaterials in two dimensions. *Phys. Rev. B* **76**, 205313 (2007).

42. K. Yokomizo, S. Murakami, Non-Bloch band theory of non-Hermitian systems. *Phys. Rev. Lett.* **123**, 066404 (2019).
43. F. K. Kunst, V. Dwivedi, Non-Hermitian systems and topology: A transfer-matrix perspective. *Phys. Rev. B* **99**, 245116 (2019).
44. E. J. Bergholtz, J. C. Budich, F. K. Kunst, Exceptional topology of non-Hermitian systems. *Rev. Mod. Phys.* **93**, 015005 (2021).
45. S. Yao, Z. Wang, Edge states and topological invariants of non-Hermitian systems. *Phys. Rev. Lett.* **121**, 086803 (2018).
46. Y. Ashida, Z. Gong, M. Ueda, Non-Hermitian physics. *Adv. Phys.* **69**, 249–435 (2020).
47. Q. Wu, X. Zhang, P. Shivasankar, Y. Chen, G. Huang, Independent flexural wave frequency conversion by a linear active metayer. *Phys. Rev. Lett.* **128**, 244301 (2022).

1

**2 Supplementary Information for
3 Active metamaterials for realizing odd mass density**

4 Qian Wu, et al

5 Yangyang Chen or Guoliang Huang.

6 E-mail: maeychen@ust.hk or huangg@missouri.edu

7 This PDF file includes:

8 Supplementary text

9 Figs. S1 to S16

10 Legends for Movies S1 to S4

11 SI References

12 Other supplementary materials for this manuscript include the following:

13 Movies S1 to S4

14 **Supporting Information Text**

15 **A. Homogenization of the odd-mass-density unit cell.** Effective properties of the odd mass meta-
 16 material are obtained at the homogenization limit. The frequency-dependent effective mass density
 17 tensor is numerically obtained using COMSOL Multiphysics solid mechanics module by imposing a
 18 prescribed displacement \mathbf{u}_P at the boundaries such that

19
$$\mathbf{F}^R = -\omega^2 V \begin{pmatrix} \hat{\rho}_{11} & \hat{\rho}_{12} \\ \hat{\rho}_{21} & \hat{\rho}_{22} \end{pmatrix} \mathbf{u}_P, \quad [1]$$

20 where \mathbf{F}^R , ω and V denote the boundary reaction forces, operating frequency and unit cell volume,
 21 respectively (1). For instance, with the application of $\mathbf{u}_P = (1, 0)^T$ at the boundaries, integrating the
 22 reaction forces \mathbf{F}_x^R and \mathbf{F}_y^R allows to determine the entries $\hat{\rho}_{11}$ and $\hat{\rho}_{21}$ using Eq. 1. The parametric
 23 study shown in Figs. S1B and S1C indicate that the magnitude and phase of the odd mass $\hat{\rho}_{12}$ linearly
 24 scale with those of the transfer function H , suggesting the linearity of the odd mass metamaterial.

25 The retrieval of elasticity tensor \mathbf{C} for the odd mass metamaterial requires specific boundary
 26 conditions (2, 3). In the retrieval, at all the boundaries we apply a global strain field $\mathbf{u}_{pre} = \mathbf{E} \mathbf{r} e^{i\omega t}$,
 27 where \mathbf{r} denotes the position vector of each discrete meshing point on the boundaries and

28
$$\mathbf{E} = \begin{pmatrix} E_{11}^0 & E_{12}^0 \\ E_{21}^0 & E_{22}^0 \end{pmatrix}. \quad [2]$$

Accordingly, the prescribed strain fields are given, respectively, by

$$\mathbf{E}_1 = \begin{pmatrix} 1 & 0 \\ 0 & 0 \end{pmatrix} \mathbf{r}, \quad [3]$$

$$\mathbf{E}_2 = \begin{pmatrix} 0 & 1 \\ 0 & 0 \end{pmatrix} \mathbf{r}, \quad [4]$$

$$\mathbf{E}_3 = \begin{pmatrix} 0 & 0 \\ 1 & 0 \end{pmatrix} \mathbf{r}, \quad [5]$$

$$\mathbf{E}_4 = \begin{pmatrix} 0 & 0 \\ 0 & 1 \end{pmatrix} \mathbf{r}. \quad [6]$$

29 The resulting stress is evaluated by the integration of the corresponding reaction forces at all the
 30 boundaries of the unit cell. The 16 entries of \mathbf{C} are determined by establishing 16 equations from
 31 the selection of the prescribed global strain and evaluated stress.

32 The unit cell for the realization of phase transition and 2D wave manipulation in Fig. 6 of the
 33 main text is illustrated here in Fig. S2A. Similar to the unit cell shown in S1 and in Figs. 2 and 3
 34 of the main text, the effective mass density tensor has nonzero odd mass density $\hat{\rho}_{12}$; also see Fig.
 35 S2B. Here, the transfer function is selected as $H = 1$, and only one resonance is seen across the
 36 frequency range, simply due to that the C4 symmetry of the unit cell yields $\hat{\rho}_{11} = \hat{\rho}_{22}$. Also, $\hat{\rho}_{12}$ is
 37 nonzero everywhere and reaches maximum at the resonance, whereas $\hat{\rho}_{21}$ remains nearly vanishing
 38 across the considered range, achieving the odd mass density. Meanwhile, the metamaterial admits
 39 an orthotropic stiffness tensor and is governed by the Hooke's law stating $\sigma_{ij} = C_{ijkl} \epsilon_{kl}$ where ϵ_{kl} is
 40 the displacement gradient. The stiffness constants are found numerically to be $C_{1111} = C_{2222} = 88.13$
 41 GPa, $C_{1122} = C_{2211} = 27.61$ GPa, $C_{1212} = C_{2121} = 26.67$ GPa, and $C_{1221} = C_{2112} = 26.32$ GPa in
 42 Voigt notation at 16 kHz using the mentioned homogenization method (1, 2). Interestingly, the odd
 43 mass causes some minor stress asymmetry, possibly due to the existence of the asymmetric control
 44 (4, 5). The couplings between the normal and shear components are five-order smaller and hence
 45 are ignored.

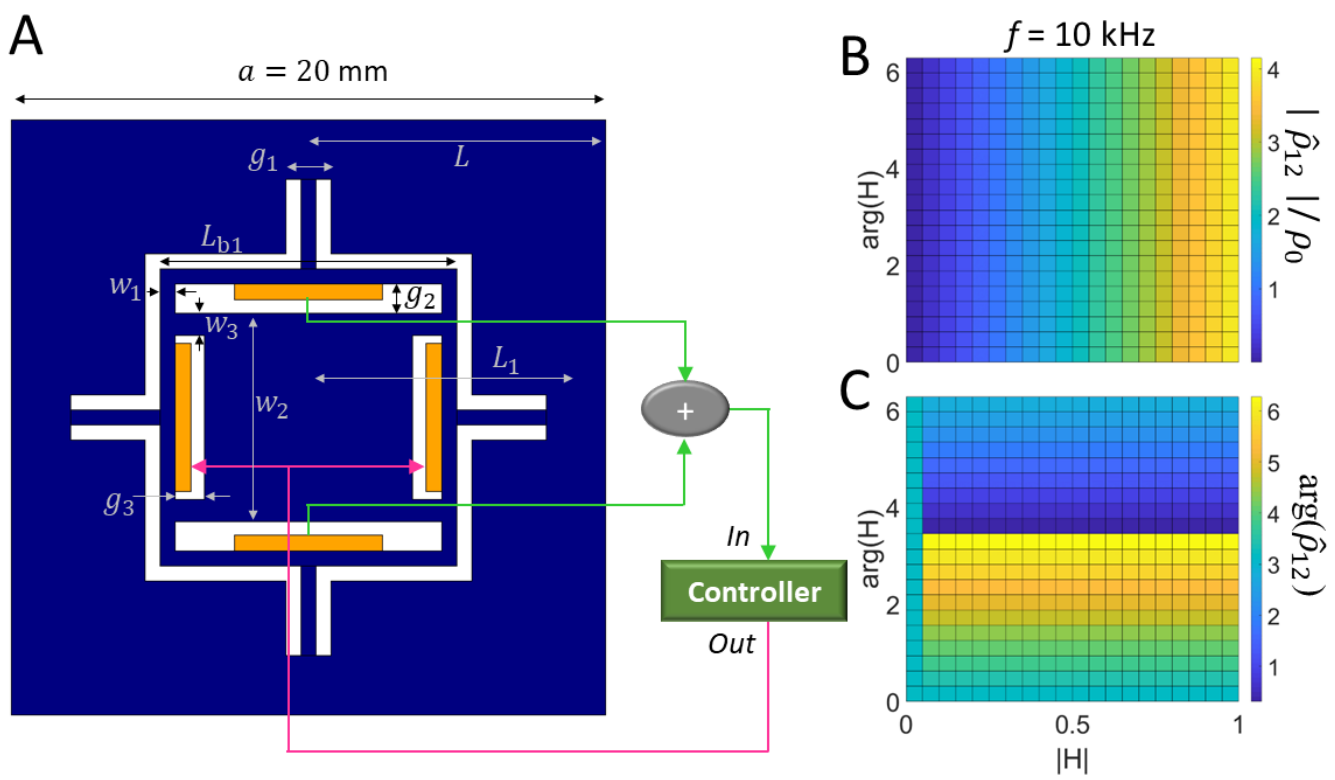


Fig. S1. (A) Design of the unit cell for 1D nonreciprocal wave coupling. The dimensions are $L = a/2 = 10$ mm, $L_1 = 9$ mm, $L_{b1} = 10$ mm, $w_1 = 0.5$ mm, $w_2 = 7$ mm, $w_3 = 0.75$ mm, $g_1 = 1.5$ mm, and $g_2 = g_3 = 1$ mm. The four piezoelectric patches (PZT-5A, 5 mm \times 0.55 mm \times 0.55 mm) are highlighted in blue. (B) Dependence of the normalized magnitude $|\hat{\rho}_{12}|/\hat{\rho}_0$ on $\arg(H)$ and $|H|$, where ρ_0 denotes the static principal mass density. (C) Dependence of the phase $\arg(\hat{\rho}_{12})$ on $\arg(H)$ and $|H|$. The results are considered at 10 kHz.

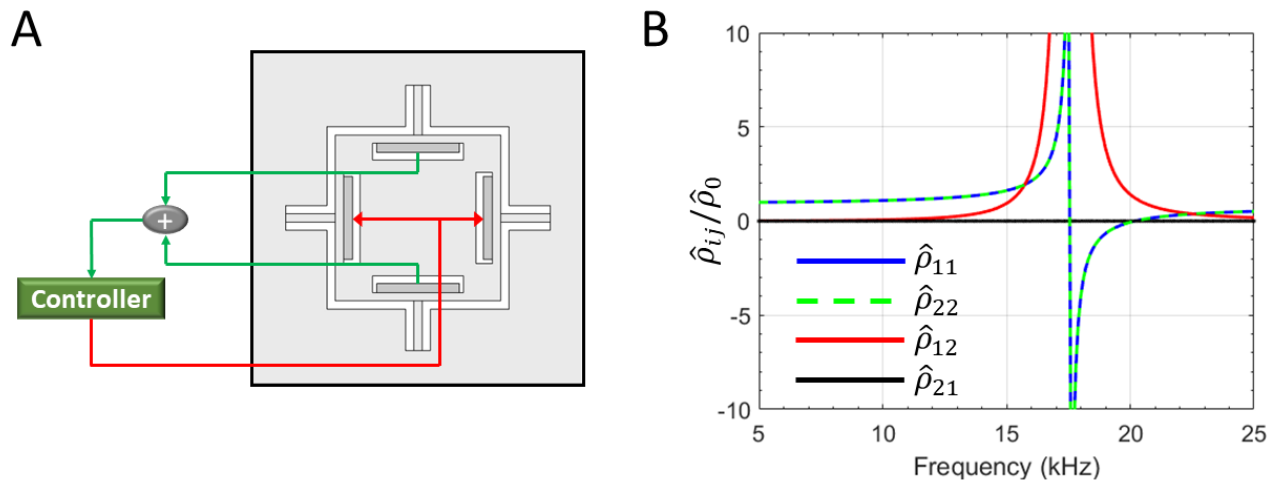


Fig. S2. (A) Design of the unit cell for the investigation of the energy phase transition and 2D wave manipulation. (B) Numerically determined entries of the effective mass density tensor $\hat{\rho}_{ij}$.

B. Characterizations of odd-mass-induced wave manipulation in one and two dimensions. To start with, we utilize the transfer matrix method to analytically derive the transmission for the one-dimensional nonreciprocal wave coupling phenomenon. The unit cell design is shown in Fig. S2A. The wave numbers read

$$q_l = \sqrt{\rho_b \omega^2 / E_b}, \quad [7]$$

$$q_b = (\rho_b A \omega^2 / D)^{1/4}, \quad [8]$$

$$q_{lm} = \sqrt{\rho_b \omega^2 / E_m}, \quad [9]$$

$$q_{bm} = (\rho_b A_0 \omega^2 / D_{b0})^{1/4}, \quad [10]$$

$$q_{lm1} = \sqrt{\rho_{b1} \omega^2 / E_{m1}}. \quad [11]$$

where

$$D_{b2} = 2D_{b0}, \quad [12]$$

$$K_b = E_b A, \quad [13]$$

$$K_m = E_m A_0, \quad [14]$$

$$K_1 = E_{m1} A. \quad [15]$$

46 At $x = -L$ and $x_1 = -L_1$.

$$47 \quad \mathbf{M0}_n = \begin{bmatrix} 1 & 1 & 0 & 0 & 0 & 0 \\ iq_l K_b & -iq_l K_b & 0 & 0 & 0 & 0 \\ 0 & 0 & 1 & 1 & 1 & 1 \\ 0 & 0 & iq_b & -iq_b & q_b & -q_b \\ 0 & 0 & -q_b^2 D & -q_b^2 D & q_b^2 D & q_b^2 D \\ 0 & 0 & -iq_b^3 D & iq_b^3 D & q_b^3 D & -q_b^3 D \end{bmatrix} \begin{bmatrix} e^{-iq_l L_1} \\ e^{iq_l L_1} \\ e^{-iq_b L} \\ e^{iq_b L} \\ e^{-q_b L} \\ e^{q_b L} \end{bmatrix} \quad [16]$$

$$48 \quad \mathbf{M}_{1n} = \begin{bmatrix} 1 & 1 & 0 & 0 & 0 & 0 \\ iq_{lm1} K_1 & -iq_{lm1} K_1 & 0 & 0 & 0 & 0 \\ 0 & 0 & 1 & 1 & 1 & 1 \\ 0 & 0 & iq_{bm} & -iq_{bm} & q_{bm} & -q_{bm} \\ 0 & 0 & -q_{bm}^2 D_{b2} & -q_{bm}^2 D_{b2} & q_{bm}^2 D_{b2} & q_{bm}^2 D_{b2} \\ 0 & 0 & -iq_{bm}^3 D_{b2} & iq_{bm}^3 D_{b2} & q_{bm}^3 D_{b2} & -q_{bm}^3 D_{b2} \end{bmatrix} \begin{bmatrix} e^{-iq_{lm1} L_1} \\ e^{iq_{lm1} L_1} \\ e^{-iq_{bm} L} \\ e^{iq_{bm} L} \\ e^{-q_{bm} L} \\ e^{q_{bm} L} \end{bmatrix} \quad [17]$$

$$49 \quad \mathbf{N}_{1n} = \begin{bmatrix} 0 & 0 & 0 & 0 & 0 & 0 \\ 0 & 0 & 0 & 0 & 0 & 0 \\ 0 & 0 & 0 & 0 & 0 & 0 \\ 0 & 0 & 0 & 0 & 0 & 0 \\ 0 & 0 & 0 & 0 & i K_m d q_{lm} e^{-iq_{lm} L} & -i K_m d q_{lm} e^{iq_{lm} L} \\ 0 & 0 & 0 & 0 & -K_m d q_{lm}^2 e^{-iq_{lm} L} & -K_m d q_{lm}^2 e^{iq_{lm} L} \end{bmatrix} \quad [18]$$

50 At $x = L$ and $x_1 = L_1$.

$$51 \quad \mathbf{M0}_p = \begin{bmatrix} 1 & 1 & 0 & 0 & 0 & 0 \\ iq_l K_b & -iq_l K_b & 0 & 0 & 0 & 0 \\ 0 & 0 & 1 & 1 & 1 & 1 \\ 0 & 0 & iq_b & -iq_b & q_b & -q_b \\ 0 & 0 & -q_b^2 D & -q_b^2 D & q_b^2 D & q_b^2 D \\ 0 & 0 & -iq_b^3 D & iq_b^3 D & q_b^3 D & -q_b^3 D \end{bmatrix} \begin{bmatrix} e^{iq_l L_1} \\ e^{-iq_l L_1} \\ e^{iq_b L} \\ e^{-iq_b L} \\ e^{q_b L} \\ e^{-q_b L} \end{bmatrix} \quad [19]$$

52

$$\mathbf{M}_{1p} = \begin{bmatrix} 1 & 1 & 0 & 0 & 0 & 0 \\ iq_{lm1}K_1 & -iq_{lm1}K_1 & 0 & 0 & 0 & 0 \\ 0 & 0 & 1 & 1 & 1 & 1 \\ 0 & 0 & iq_{bm} & -iq_{bm} & q_{bm} & -q_{bm} \\ 0 & 0 & -q_{bm}^2 D_{b2} & -q_{bm}^2 D_{b2} & q_{bm}^2 D_{b2} & q_{bm}^2 D_{b2} \\ 0 & 0 & -iq_{bm}^3 D_{b2} & iq_{bm}^3 D_{b2} & q_{bm}^3 D_{b2} & -q_{bm}^3 D_{b2} \end{bmatrix} \begin{bmatrix} e^{iq_{lm1}L_1} \\ e^{-iq_{lm1}L_1} \\ e^{iq_{bm}L} \\ e^{-iq_{bm}L} \\ e^{q_{bm}L} \\ e^{-q_{bm}L} \end{bmatrix} [20]$$

53

$$\mathbf{N}_{1p} = \begin{bmatrix} 0 & 0 & 0 & 0 & 0 & 0 \\ 0 & 0 & 0 & 0 & 0 & 0 \\ 0 & 0 & 0 & 0 & 0 & 0 \\ 0 & 0 & 0 & 0 & 0 & 0 \\ 0 & 0 & 0 & 0 & iK_m dq_{lm} e^{iq_{lm}L} & -iK_m dq_{lm} e^{-iq_{lm}L} \\ 0 & 0 & 0 & 0 & -K_m dq_{lm}^2 e^{iq_{lm}L} & -K_m dq_{lm}^2 e^{-iq_{lm}L} \end{bmatrix} [21]$$

54 At $x = 0$.

55

$$\mathbf{M}_{10} = \begin{bmatrix} 1 & 1 & 0 & 0 & 0 & 0 \\ iq_{lm1}K_1 & -iq_{lm1}K_1 & 0 & 0 & 0 & 0 \\ 0 & 0 & 1 & 1 & 1 & 1 \\ 0 & 0 & iq_{bm} & -iq_{bm} & q_{bm} & -q_{bm} \\ 0 & 0 & -q_{bm}^2 D_{b2} & -q_{bm}^2 D_{b2} & q_{bm}^2 D_{b2} & q_{bm}^2 D_{b2} \\ 0 & 0 & -iq_{bm}^3 D_{b2} & iq_{bm}^3 D_{b2} & q_{bm}^3 D_{b2} & -q_{bm}^3 D_{b2} \end{bmatrix} [22]$$

56

$$\mathbf{N}_{10} = \begin{bmatrix} 0 & 0 & 0 & 0 & 0 & 0 \\ 0 & 0 & 0 & 0 & 0 & 0 \\ 0 & 0 & 0 & 0 & 0 & 0 \\ 0 & 0 & 0 & 0 & 0 & 0 \\ 0 & 0 & 0 & 0 & 0 & 0 \\ 0 & 0 & 0 & 0 & -K_m dq_{lm}^2 & -K_m dq_{lm}^2 \end{bmatrix} [23]$$

57

$$\mathbf{T}_1 = \begin{bmatrix} 1 & 1 & -1 & -1 \\ iq_{lm} K_m d^2 & -iq_{lm} K_m d^2 & -iq_{lm} K_m d^2 & iq_{lm} K_m d^2 \\ e^{-iq_{lm}L} & e^{iq_{lm}L} & 0 & 0 \\ 0 & 0 & e^{iq_{lm}L} & e^{-iq_{lm}L} \end{bmatrix} [24]$$

58

$$\mathbf{T}_2 = \begin{bmatrix} 0 & 0 & 0 & 0 \\ e^{-iq_{bm}L} \omega^2 m_I / L & e^{iq_{bm}L} \omega^2 m_I / L & e^{-q_{bm}L} \omega^2 m_I / L & e^{q_{bm}L} \omega^2 m_I / L \\ -iq_{bm} e^{-iq_{bm}L} & iq_{bm} e^{iq_{bm}L} & -q_{bm} e^{-q_{bm}L} & q_{bm} e^{q_{bm}L} \\ 0 & 0 & 0 & 0 \\ -e^{iq_{bm}L} \omega^2 m_I / L & -e^{-iq_{bm}L} \omega^2 m_I / L & -e^{q_{bm}L} \omega^2 m_I / L & -e^{-q_{bm}L} \omega^2 m_I / L \\ 0 & 0 & 0 & 0 \\ -iq_{bm} e^{iq_{bm}L} & iq_{bm} e^{-iq_{bm}L} & -q_{bm} e^{q_{bm}L} & q_{bm} e^{-q_{bm}L} \end{bmatrix} [25]$$

59

$$\mathbf{Tn} = \mathbf{T}_1^{-1} \mathbf{T}_2. [26]$$

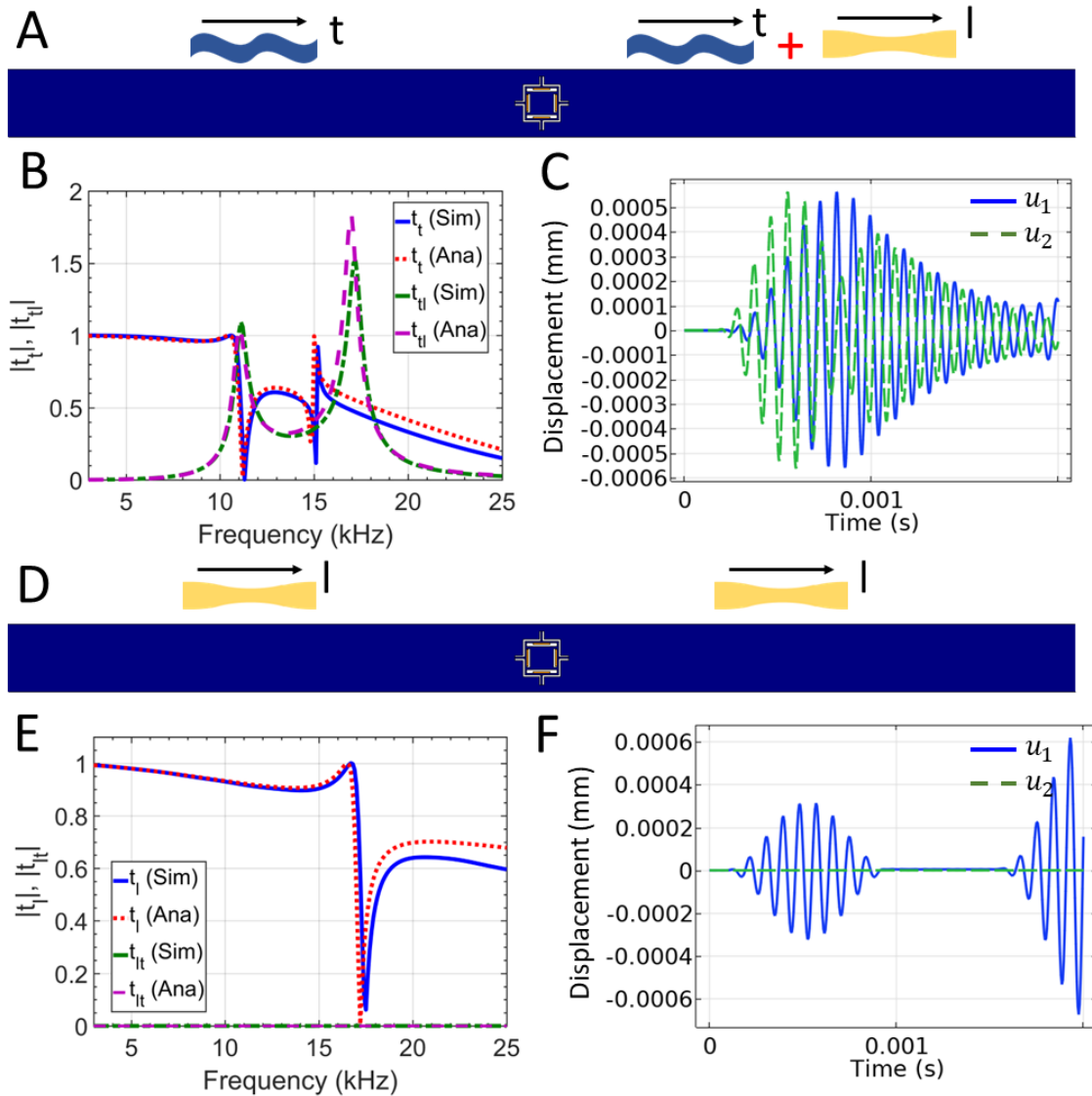
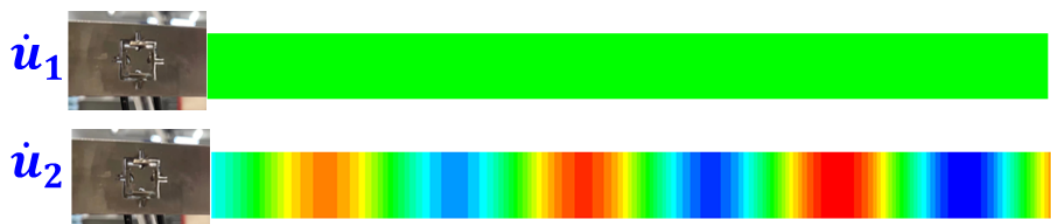


Fig. S3. One-dimensional nonreciprocal wave coupling. (A) Schematic of the transverse incidence. (B) Analytical and numerical comparison for both transmissions. (C) Transient analysis results for the output displacements u and v for longitudinal and transverse modes, respectively. (D) Schematic of the longitudinal incidence. (E) Analytical and numerical comparison for both transmissions. (F) Transient analysis results for the output displacements u and v for longitudinal and transverse modes, respectively.

Without control



With control

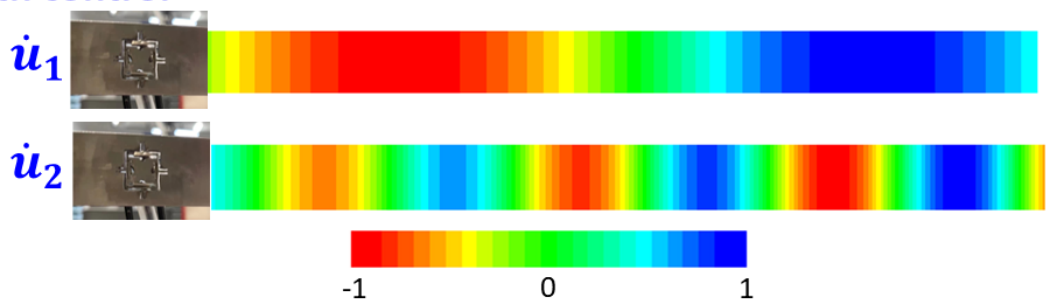


Fig. S4. Experimentally measured normalized velocity field distributions for one-dimensional nonreciprocal wave coupling. The output velocities \dot{u}_1 and \dot{u}_2 for longitudinal and transverse modes are displayed without and with the active control.

$$\mathbf{Tn}_{f11}(5 : 6, 3 : 6) = \mathbf{Tn}(1 : 2, 1 : 4), \quad [27]$$

$$\mathbf{Tn}_{f12}(5 : 6, 3 : 6) = \mathbf{Tn}(1 : 2, 5 : 8), \quad [28]$$

$$\mathbf{Tn}_{f21}(5 : 6, 3 : 6) = \mathbf{Tn}(3 : 4, 1 : 4), \quad [29]$$

$$\mathbf{Tn}_{f22}(5 : 6, 3 : 6) = \mathbf{Tn}(3 : 4, 5 : 8). \quad [30]$$

60 The rest entries of \mathbf{Tn} are zeros.

$$61 \quad \mathbf{F} = \begin{bmatrix} 0 & 0 & 0 & 0 & 0 & 0 \\ \omega^2 \hat{\rho}_{11} & \omega^2 \hat{\rho}_{11} & \omega^2 \hat{\rho}_{12} & \omega^2 \hat{\rho}_{12} & \omega^2 \hat{\rho}_{12} & \omega^2 \hat{\rho}_{12} \\ 0 & 0 & 0 & 0 & 0 & 0 \\ 0 & 0 & 0 & 0 & 0 & 0 \\ 0 & 0 & 0 & 0 & 0 & 0 \\ -\omega^2 \hat{\rho}_{21} & -\omega^2 \hat{\rho}_{21} & -\omega^2 \hat{\rho}_{22} & -\omega^2 \hat{\rho}_{22} & -\omega^2 \hat{\rho}_{22} & -\omega^2 \hat{\rho}_{22} \end{bmatrix} \quad [31]$$

$$62 \quad \mathbf{M1}_n = \mathbf{M}_{1n} + 2\mathbf{N}_{1n}\mathbf{Tn}_{f11}, \quad [32]$$

$$63 \quad \mathbf{M1}_p = \mathbf{M}_{1p} + 2\mathbf{N}_{1p}\mathbf{Tn}_{f22}, \quad [33]$$

$$\mathbf{M1}_{0n1} = \mathbf{M}_{10} + 2\mathbf{N}_{10}\mathbf{Tn}_{f11} - 2\mathbf{N}_{10}\mathbf{Tn}_{f21} - \mathbf{F}, \quad [34]$$

$$64 \quad \mathbf{M1}_{0n2} = \mathbf{M}_{10} + 2\mathbf{N}_{10}\mathbf{Tn}_{f11} - 2\mathbf{N}_{10}\mathbf{Tn}_{f12} \quad [35]$$

65 The total transfer matrix reads

$$66 \quad \mathbf{T} = \mathbf{M0}_n^{-1}(\mathbf{M1}_n\mathbf{M1}_{0n1}^{-1}\mathbf{M1}_{0n2} + 2\mathbf{N}_{1n}\mathbf{Tn}_{f12})(\mathbf{M1}_p + 2\mathbf{N}_{1p}\mathbf{Tn}_{f21}\mathbf{M1}_{0n1}^{-1}\mathbf{M1}_{0n2})^{-1}\mathbf{M0}_p \quad [36]$$

67 To numerically demonstrate the nonreciprocal wave coupling, we show the exactly same beam in
 68 the main text with incidences of two different polarization, namely transverse (t) and longitudinal
 69 (l) excitation. The results shown in Figs. S3B and S3C are identical with those presented in Fig.
 70 3 of the main text, showing the conversion of $t \rightarrow l$. To compare with the longitudinal incidence,
 71 we conduct frequency-domain and transient simulations for the case shown in Fig. S3D. The
 72 corresponding results are illustrated in Figs. S3E and S3F. It is seen that the longitudinal incidence
 73 does not generate any transverse transmission. In other words, the conversion of $l \rightarrow t$ is forbidden,
 74 numerically proving the nonreciprocal wave coupling. In both cases, the results obtained using
 75 numerical simulations and transfer matrix method (Eq. 36) agree very well.

76 In Fig. S4, the experimentally measured \dot{u}_1 and \dot{u}_2 field distributions are present with the toggle
 77 of the active control. The field intensities are normalized with their own maximums. It is clearly
 78 seen that with the active control, the odd mass is turned on, and the transverse incidence generates
 79 non-vanishing longitudinal transmission. By contrast, without the active control, no longitudinal
 80 wave is generated at the output. In Figs. S5 and S6, the circuit design of the odd-mass unit cell and
 81 PZT transducer for exciting transverse incidence are preset (6).

82 Figure S7 shows the numerically calculated transmission coefficients for both longitudinal (Fig.
 83 S7A) and transverse (Fig. S7B) incidences with an odd-mass unit rotated by 90 degrees. It can
 84 be easily seen from (Fig. S7A) that a longitudinal incidence can generate transverse transmission
 85 around the first resonance (10.9 kHz) because the sensing pairs are along the horizontal direction
 86 compared to the original case shown in the manuscript. On the contrary, as shown in from (Fig.
 87 S7B), a transverse incidence cannot generate any longitudinal transmission across the frequency

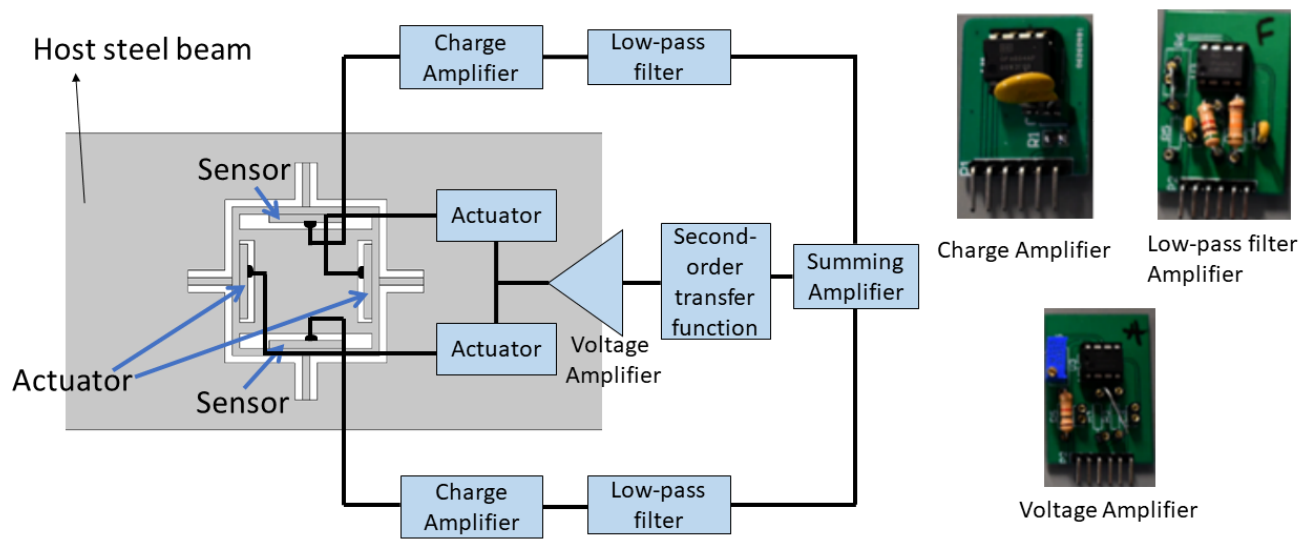


Fig. S5. Circuit diagram of the unit cell for the nonreciprocal wave coupling. The resulting transfer function reads $H(\omega) = H_0 / (\omega^2 / \omega_0^2 + 2\xi\omega / \omega_0 + 1)$, where $H_0 = 2 \times 10^8$, $\xi = 0.5$ and $\omega_0 = 2\pi \times 15$ kHz. The circuit diagrams for the three components are shown in Fig. S12.

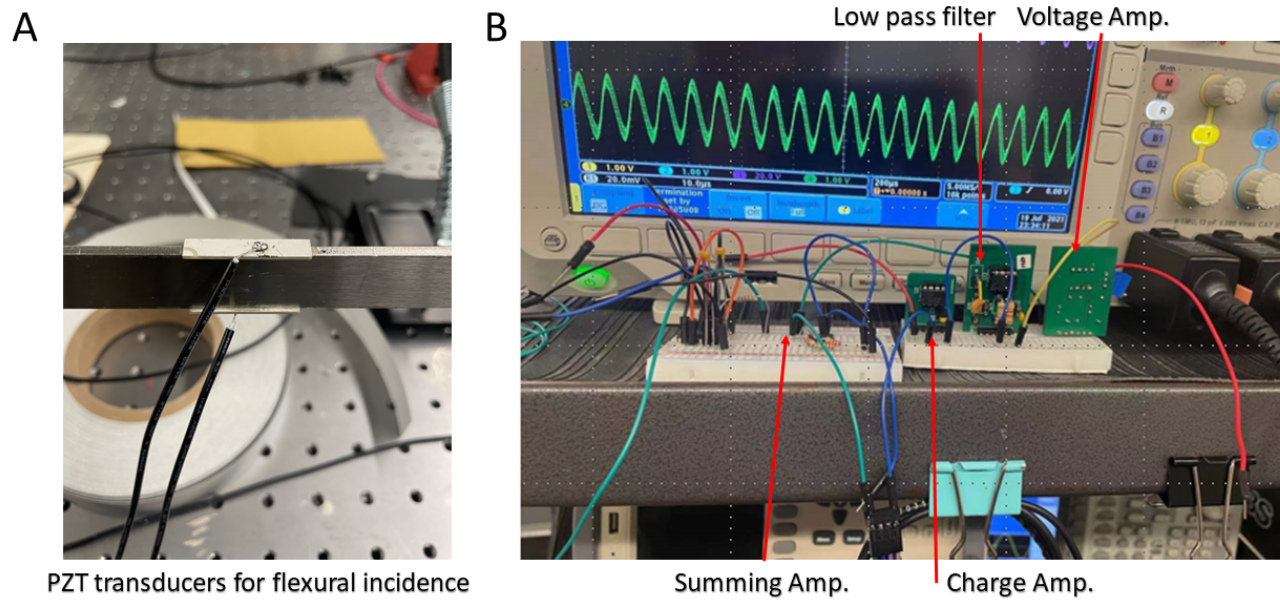


Fig. S6. (A) The photo of the PZT transducer which consists of two PZT-5A patches placed in parallel. This arrangement allows to generate transverse incidence. (B) The photo of the electrical control circuits, including low pass filter, voltage amplifier, summing amplifier and charge amplifier.

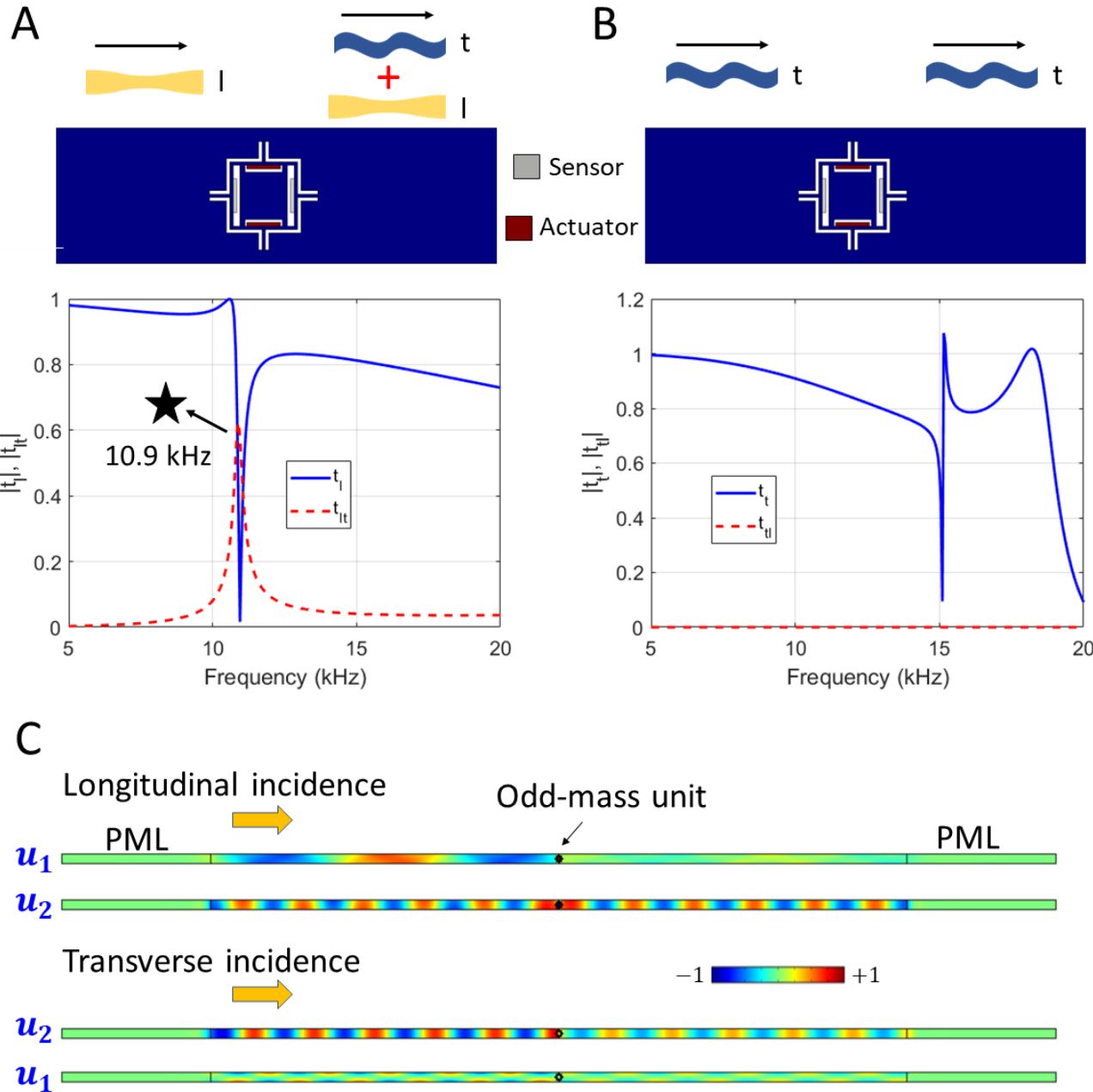


Fig. S7. Nonsymmetric wave coupling with an odd-mass unit rotated by 90 degrees. (A) The rotated metamaterial unit cell that exhibits odd mass can generate both longitudinal and transverse transmission upon a longitudinal incidence. The blue and red curves denote the transmission coefficients of longitudinal-longitudinal (t_{ll}) and longitudinal-transverse (t_{lt}), respectively. (B) The rotated unit can only generate transverse transmission upon a transverse incidence. The blue and red curves denote the transmission coefficients of transverse-transverse (t_t) and transverse-longitudinal (t_{tl}), respectively. (C) Numerically obtained field distributions under both incidences at $\omega = 2\pi \times 10$ kHz. The field distributions are all normalized with their own maximums. In the simulations, the ratio of transfer function and reference capacitance is selected as $H/C_0 = 2 \times 10^{12} F^{-1}$.

range due to the absence of sensing components along the vertical direction. The corresponding normalized field distributions are listed in (Fig. S7C), confirming the nonsymmetric wave coupling behavior by the odd mass. This nonreciprocal behavior is a consequence of the nonconservative force required by the emergent odd mass density property. Therefore, the 1D experiments are appropriate for validating the existence of the odd mass density in the proposed active solids.

Here, in Fig. S8 we also provide the comparison for the presented cases shown in Fig. 6 of the main text. We find some non-negligible discrepancies between the effective media and real structures in the energy-unbroken phase, i.e. $\hat{\beta} = 0$ and $\hat{\beta} = 0.29$. The main cause is that the implemented unit cell may not lie properly within the subwavelength regime, which in turn weakens the long-wavelength assumption to some extent.

Further, we illustrate the same comparison for $H = -1$ and $H = 1i$. The corresponding $\hat{\beta}$ become $\hat{\beta} = -1.18$ and $\hat{\beta} = 1.18i$. As can be seen in Fig. S9, the homogenized media and actual structures show satisfactory agreement. As has been discussed in the main text, $\hat{\beta} = -1.18$ results in the wave amplification at $\theta = 3\pi/4$ and $7\pi/4$ for both modes. On the contrary, $\hat{\beta} = -1.18$ results in the wave amplification at $\theta = 3\pi/4$ and $7\pi/4$ for the shear mode, but at $\theta = \pi/4$ and $5\pi/4$ for the longitudinal one.

Lastly, to demonstrate transient analysis on the 2D directional wave amplification, we finalize a unit cell design shown in Fig. S10A, which features the entries of the effective mass density tensor shown in Fig. S10B. Without loss of generality, we consider 16 kHz as the excitation frequency to demonstrate the real-time directional wave amplification induced by the odd mass in the main text.

The 2D wave propagation control in time-dependent simulations in the structured steel plate with and without active control is shown in Figs. S11A and S11B, respectively. A 10-cycle tone burst signal centered at 16 kHz is selected as the excitation signal, which gives equivalently $\hat{\rho}_{11} \approx \hat{\rho}_{22} = 4820 \text{ kg/m}^3$, $\hat{\rho}_{12} = 5370 \text{ kg/m}^3$, and $\hat{\rho}_{21} \approx 0$ (see Fig. S10B). As is shown, the wave amplification when the active control is ON can be clearly seen around $\theta_1 = \frac{\pi}{4}$ and $\frac{5\pi}{4}$ as time progresses. While the wave field distribution without the control resembles that of an isotropic medium given by $\hat{\beta} = 0$ in Fig. 5A of the main text ([SI Movies](#)). Since the selected system settings are commercially available, the transient analysis provides solid evidence for this 2D exotic wave function and effective guidance for experimental demonstration and validation.

In the experimental demonstration of the 2D directional wave amplification, the 2×2 active array has been fabricated out of a stainless steel host plate. Sensor-actuator pairs are formed by connecting horizontal and vertical piezoelectric patches through a programmable control circuit, whose circuit diagram is shown in Fig. S12.

To confirm the 2×2 active array can be effectively treated as an effective homogeneous metamaterial with odd mass density, we conduct harmonic simulations for both the real structure and effective medium scenarios. Figure S13A displays the unit cell used in the 2D experiments. Figures S13B and S13C present the numerical comparison between the real structure and the effective homogeneous medium ($\hat{\rho}_{11} = \hat{\rho}_{22} = 9126.5 + 9.8i \text{ kg/m}^3$, $\hat{\rho}_{21} \approx 0$, and $\hat{\rho}_{11} = 90884 - 30168i \text{ kg/m}^3$ at 14 kHz). Satisfactory agreement can be observed, indicating that the 2×2 active array can be effectively treated as a homogeneous metamaterial decorated with the odd mass density.

C. Reconstruction of correspondence between open boundary condition (OBC) spectrum and periodic boundary condition (PBC) spectrum on the generalized Brillouin zone (GBZ). For the Hermitian system, the OBC spectrum for infinite system size $L \rightarrow \infty$ is continuous and it is the same as the PBC spectrum for the wave number with the periodicity over the Brillouin zone. However, in the main text, we find discrepancies between the OBC and PBC spectra in the energy-broken phase

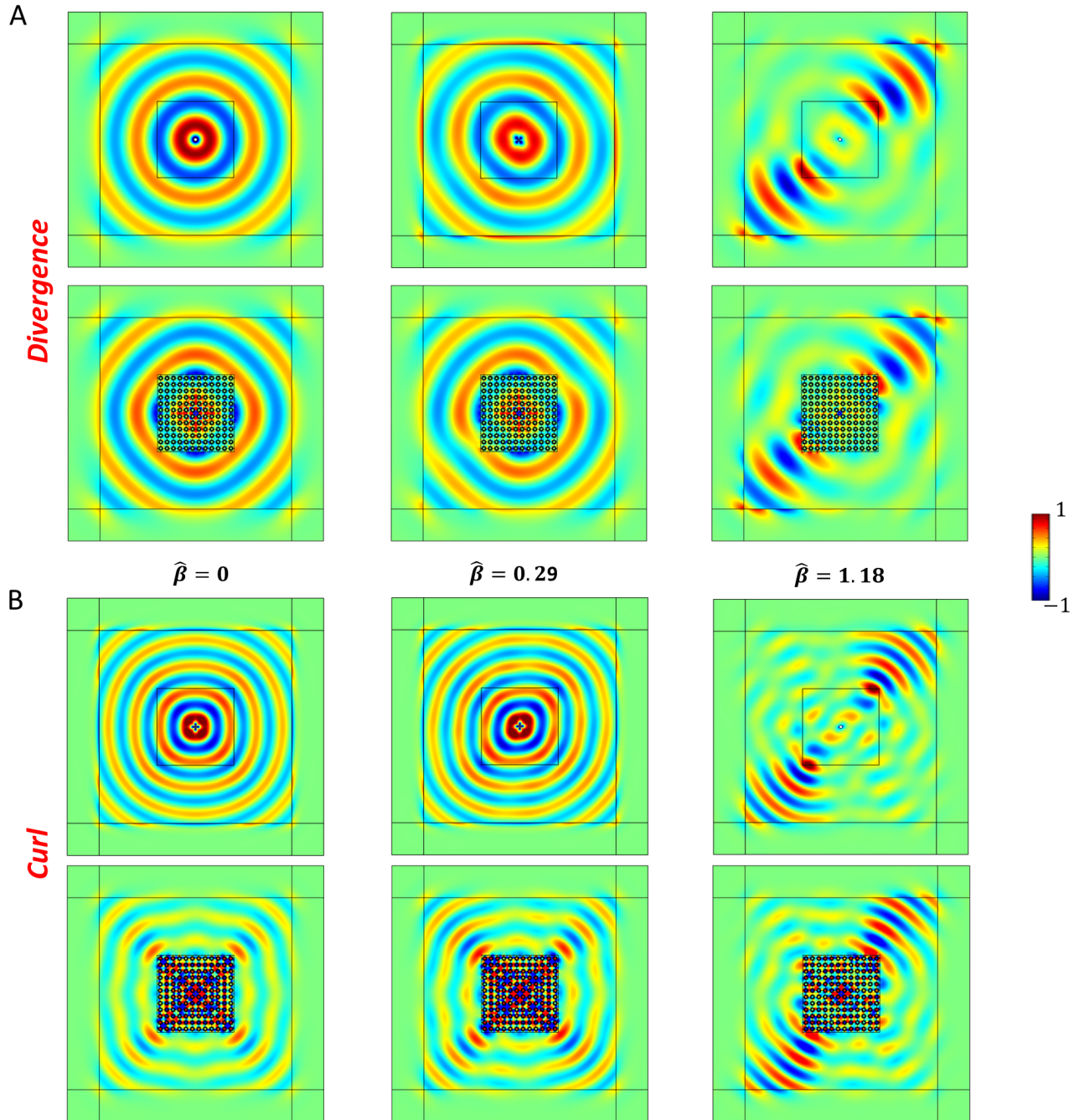


Fig. S8. Comparison between actual structures and homogenized media. (A) Numerically evaluated divergence fields of displacement at 16 kHz for various $\hat{\beta}$ under a pressure loading. (B) Numerically evaluated curl fields of displacement at 16 kHz for various $\hat{\beta}$ under a shear loading. In both (A) and (B), the top panels show the field distributions of the homogenized media, whereas the bottom panels illustrate the corresponding actual structures. The field distributions are normalized with their own maximums.

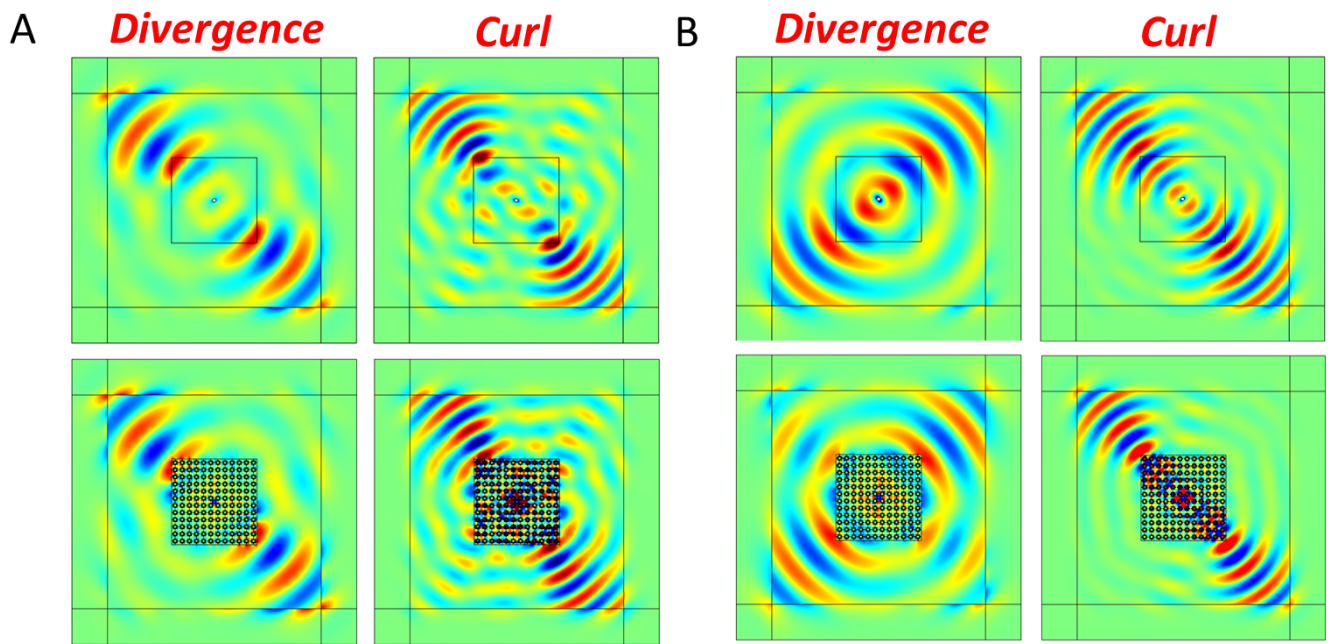


Fig. S9. Comparison between actual structures and homogenized media for tunable 2D wave beam steering. (A) Numerically evaluated divergence and curl fields of displacement at 16 kHz for $\hat{\beta} = -1.18$ under a pressure and shear loading, respectively. (B) Numerically evaluated divergence and curl fields of displacement at 16 kHz for $\hat{\beta} = 1.18i$ under a pressure and shear loading, respectively. In both (A) and (B), the top panels show the field distributions of the homogenized media, whereas the bottom panels illustrate the corresponding actual structures. The field distributions are normalized with their own maximums.

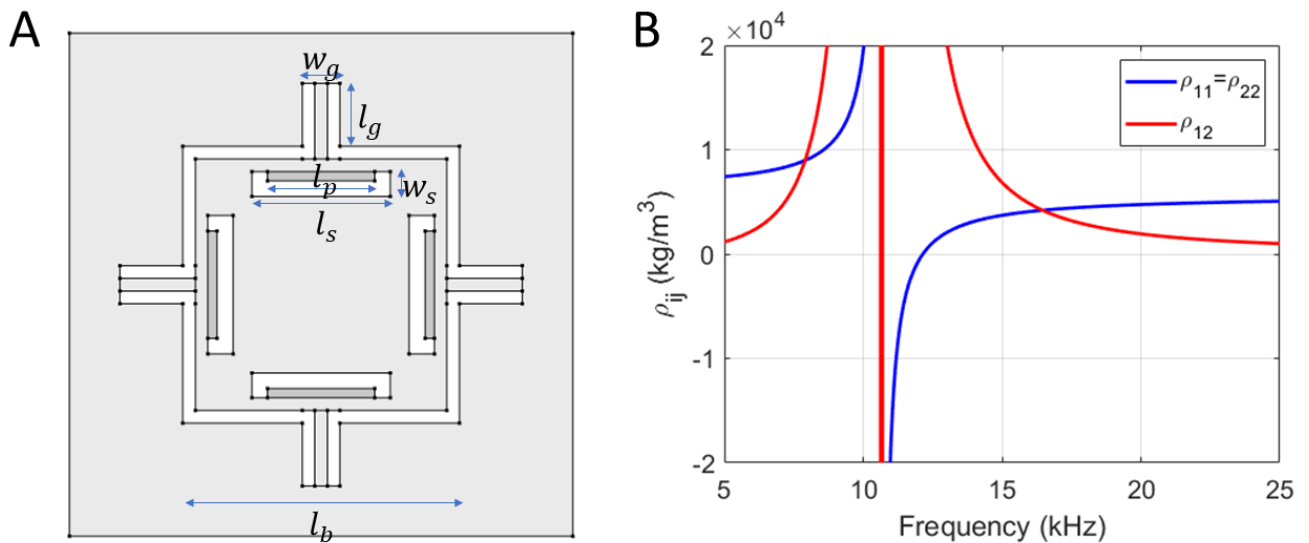


Fig. S10. (A) Schematic of the unit cell of the odd plate with the matrix material being steel (205 GPa, 7850 kg/m^3 , 0.28). The geometrical parameters are $l_p = 6.4 \text{ mm}$, $l_s = 8.3 \text{ mm}$, $w_s = 1.55 \text{ mm}$, $l_g = 3.75 \text{ mm}$, $w_g = 2.25 \text{ mm}$, and $l_b = 16.5 \text{ mm}$. The thickness of the PZT patches is $t_p = 0.55 \text{ mm}$. The lattice constant of the unit cell is 30 mm. (B) Effective mass density tensor of the unit cell in (A). At the excitation frequency 16 kHz, we have equivalently $\rho_{11} \approx \rho_{22} = 4820 \text{ kg/m}^3$, $\rho_{12} = 5370 \text{ kg/m}^3$, and $\rho_{21} = 0$.

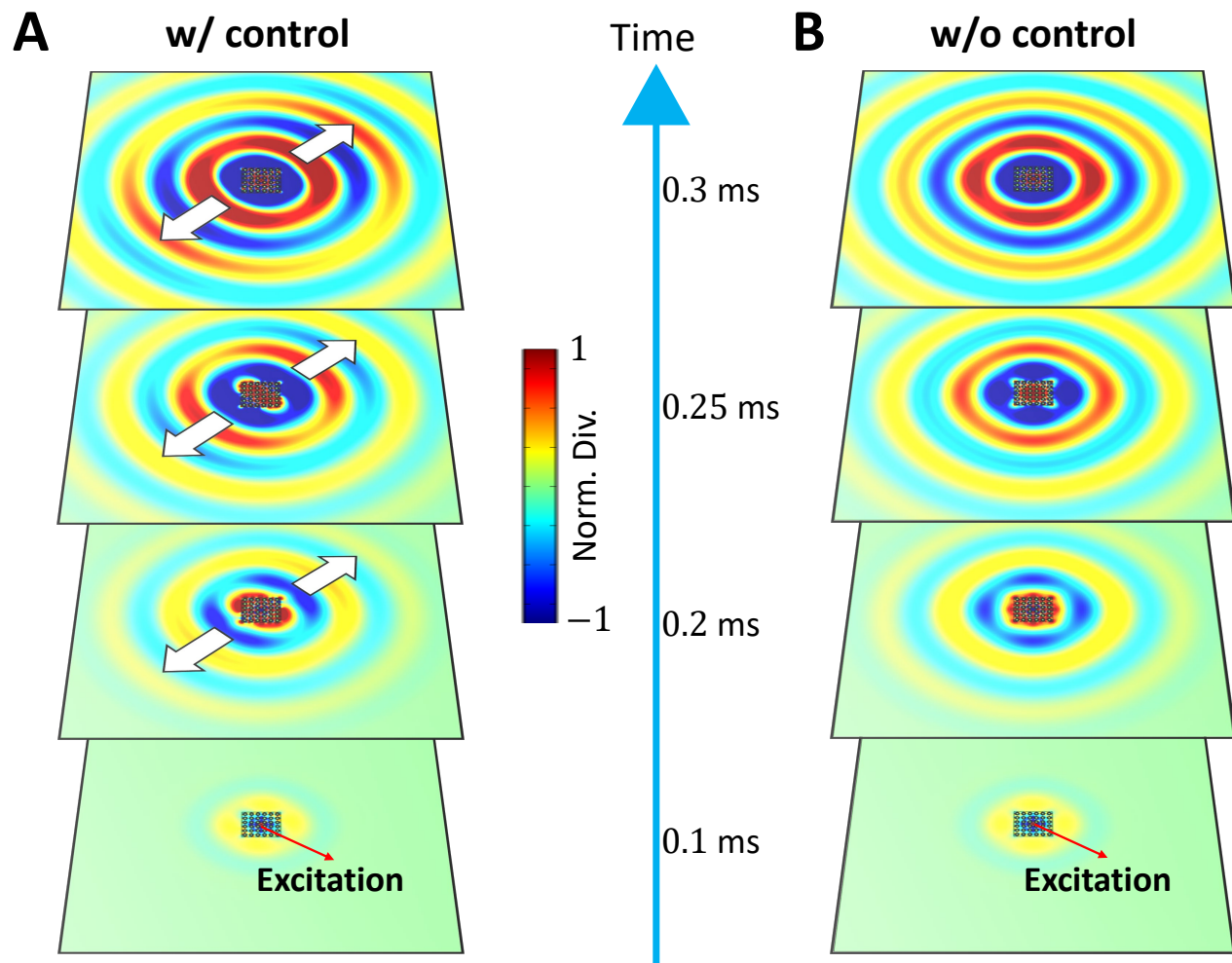


Fig. S11. Real-time illustration of longitudinal wave manipulation of the odd-mass plate (A) with and (B) without active control. The excitation is selected to be a 10-cycle tone burst signal centered at 16 kHz. The white arrows represent the wave amplification directions. The divergence field snapshots at different time instants are shown for the cases with and without active control. The field amplitudes in all figures are normalized to the amplitude maximum of case without control at $t = 0.3$ ms.

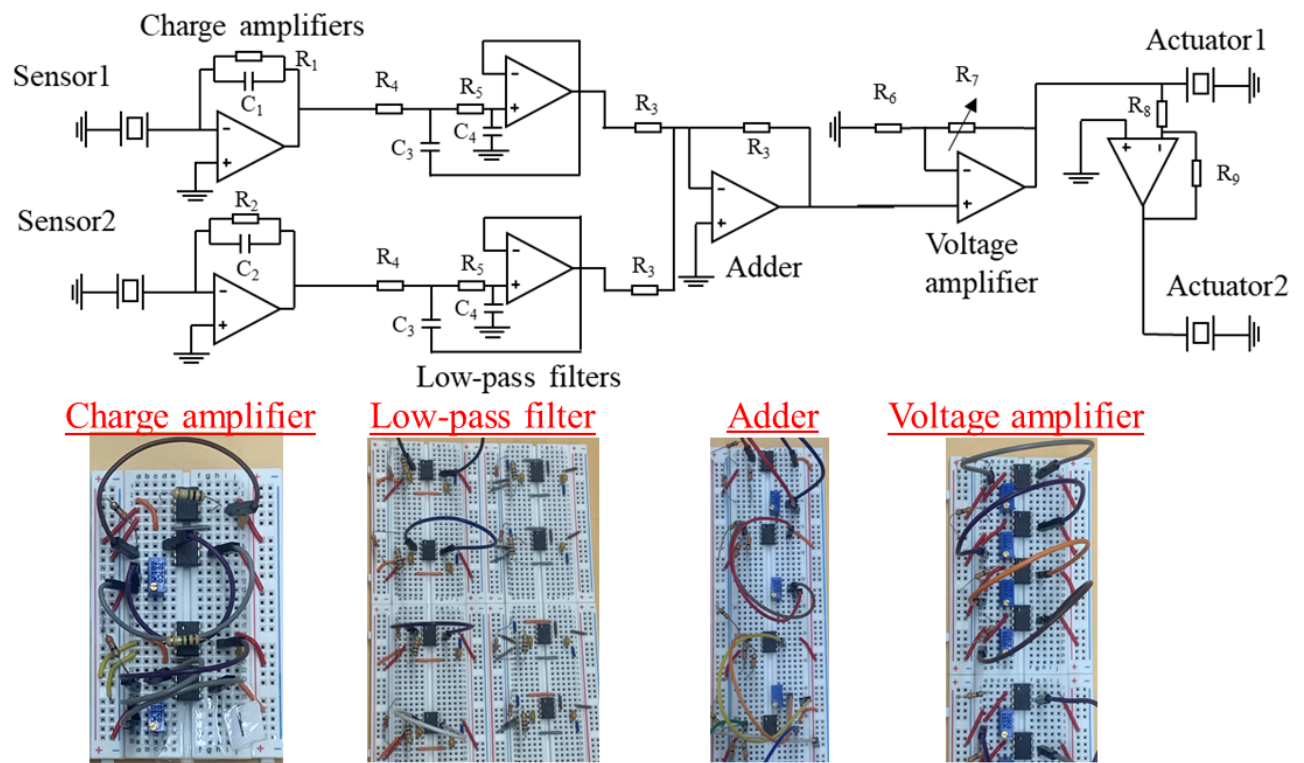


Fig. S12. Top panel: Circuit diagram used to realize the odd mass density in the experiment. The selected electrical parameters are $R_1 = 1 \text{ M}\Omega$, $R_2 = R_3 = R_6 = R_9 = R_8 = 330 \Omega$, $C_1 = C_2 = 1 \text{ nF}$, $C_3 = 0.47 \text{ nF}$, and $C_4 = 4.7 \text{ nF}$. Bottom panel: Photos of the charge amplifier, low-pass filter, adder, and voltage amplifier.

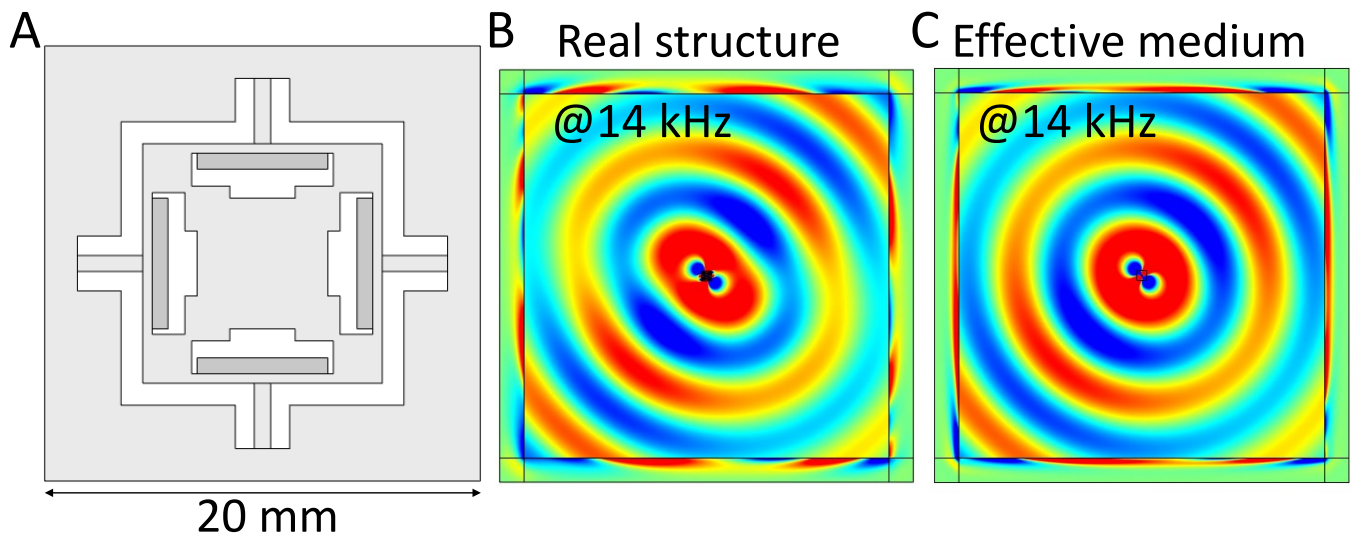


Fig. S13. (A) Unit cell used in the 2D experiment in the main text. (B,C) Comparison of the numerically obtained divergence fields between the real structure (B) and the effective homogeneous medium (C). In both scenarios, the excitation is a cylindrical longitudinal wave at the center of the metamaterial at 14 kHz. The computation domain is surrounded by perfect matched layers.

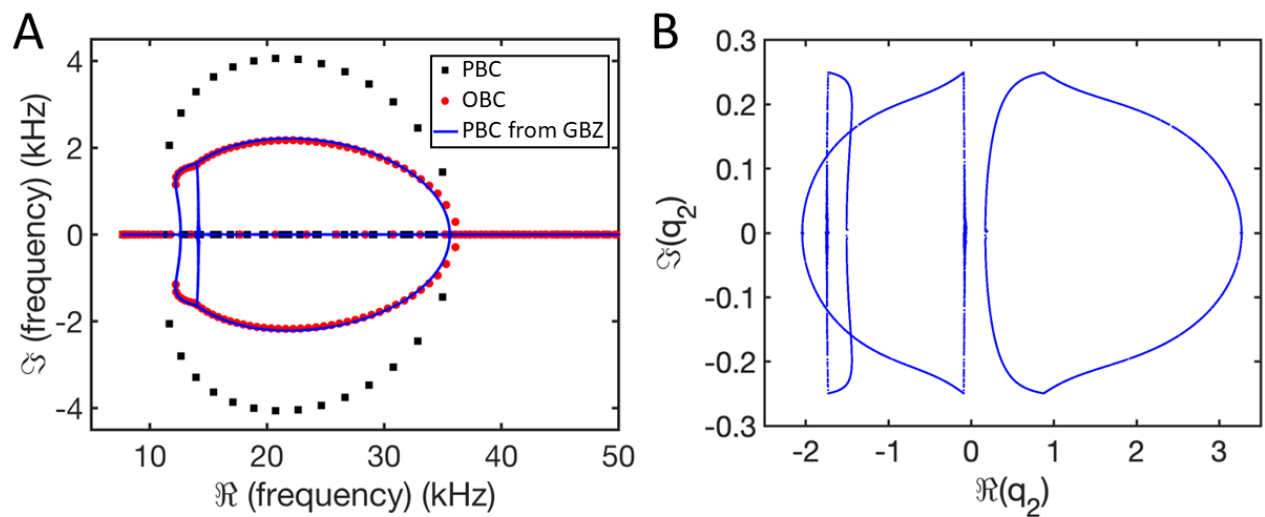


Fig. S14. Frequency spectrum and GBZ. (A) The frequency spectrum for PBC, OBC are from Fig. 8 of the main text. The PBC spectrum from GBZ is calculated using Eqs. 53 and 41. (B) Generalized Brillouin zone is calculated from Eqs. 53 and 41.

region. Here we reconstruct the correspondence between the OBC and PBC spectra by extending to a generalization Brillouin zone (GBZ). First, we derive the OBC spectrum equation, Eq. 48, of odd mass density system analytically. Then under the condition $L \rightarrow \infty$, we reduce the OBC spectrum equation to a simpler one, Eq. 53, which gives the GBZ. Substituting the wave number on the generalized Brillouin zone into the dispersion relation, we can obtain the PBC spectrum on GBZ, which would be identical to the OBC spectrum with $L \rightarrow \infty$.

For a solid with odd mass density, the equations of motion are

$$\begin{cases} \sigma_{11,1} + \sigma_{12,2} = \hat{\rho}_{11}\ddot{u} + \hat{\rho}_{12}\ddot{v} \\ \sigma_{12,1} + \sigma_{22,2} = \hat{\rho}_{22}\ddot{v}. \end{cases} \quad [37]$$

where for simplicity we have replaced (u_1, u_2) of the main text with (u, v) here. Constitutive relation for plane strain problem is

$$\begin{bmatrix} \sigma_{11} \\ \sigma_{22} \\ \sigma_{12} \end{bmatrix} = \begin{bmatrix} \lambda + 2\mu & \lambda & 0 \\ \lambda & \lambda + 2\mu & 0 \\ 0 & 0 & \mu \end{bmatrix} \begin{bmatrix} \varepsilon_{11} \\ \varepsilon_{22} \\ \varepsilon_{12} \end{bmatrix} \quad [38]$$

Substituting Eq. 38 into Eq. 37, the equations of motion expressed by displacements are

$$\begin{bmatrix} (\lambda + 2\mu)\partial_1^2 + \mu\partial_2^2 & (\lambda + \mu)\partial_1\partial_2 \\ (\lambda + \mu)\partial_1\partial_2 & (\lambda + 2\mu)\partial_2^2 + \mu\partial_1^2 \end{bmatrix} \begin{bmatrix} u \\ v \end{bmatrix} = \begin{bmatrix} \hat{\rho}_{11} & \hat{\rho}_{12} \\ 0 & \hat{\rho}_{22} \end{bmatrix} \begin{bmatrix} \ddot{u} \\ \ddot{v} \end{bmatrix} \quad [39]$$

With the substitution of the standing wave solution $u = ue^{i(q_1x_1+q_2x_2-\omega t)}$, $v = ve^{i(q_1x_1+q_2x_2-\omega t)}$ into Eq. 39, we have

$$\begin{bmatrix} (\lambda + 2\mu)q_1^2 + \mu q_2^2 & (\lambda + \mu)q_1q_2 \\ (\lambda + \mu)q_1q_2 & (\lambda + 2\mu)q_2^2 + \mu q_1^2 \end{bmatrix} \begin{bmatrix} u \\ v \end{bmatrix} = \omega^2 \begin{bmatrix} \hat{\rho}_{11} & \hat{\rho}_{12} \\ 0 & \hat{\rho}_{22} \end{bmatrix} \begin{bmatrix} u \\ v \end{bmatrix} \quad [40]$$

The vanishing of determinant gives the polynomial equation

$$c_1q_2^4 + c_2q_2^3 + c_3q_2^2 + c_4q_2 + c_5 = 0 \quad [41]$$

where the coefficients can be obtained from the expansion of determinant. Equation 41 gives four roots $q_2^1, q_2^2, q_2^3, q_2^4$ with the arrangement of $\Im(q_2^1) \leq \Im(q_2^2) \leq \Im(q_2^3) \leq \Im(q_2^4)$. Accordingly, the four corresponding eigenvectors are

$$\begin{aligned} u_i &= -(\lambda + \mu)q_q q_2 + \omega^2 \hat{\rho}_{12} \\ v_i &= (\lambda + 2\mu)q_1^2 + \mu q_2^2 - \omega^2 \hat{\rho}_{11}, \quad i = 1, 2, 3, 4. \end{aligned} \quad [42]$$

The superposition of the eigenstates gives the general solution

$$\begin{bmatrix} u \\ v \end{bmatrix} = \sum_{i=1}^4 C_i e^{iq_2^i x_2} \begin{bmatrix} u_i \\ v_i \end{bmatrix} \quad [43]$$

Here, we consider the system to be infinite along the x_1 direction. While along the x_2 direction, we impose OBCs (stress free boundary conditions) which are

$$\begin{cases} \sigma_{22}|_{x_2=0} = 0 \\ \sigma_{11}|_{x_2=0} = 0, \end{cases} \quad \begin{cases} \sigma_{21}|_{x_2=L} = 0 \\ \sigma_{12}|_{x_2=L} = 0. \end{cases} \quad [44]$$

¹⁵⁷ With the substitution of the constitutive relation, they become

$$\begin{aligned} & [\lambda u_{,1} + (\lambda + 2\mu) v_{,2}] |_{x_2=0} = 0 \\ & (u_{,2} + v_{,1}) |_{x_2=0} = 0 \end{aligned} \quad [45]$$

¹⁵⁹ and

$$\begin{aligned} & [\lambda u_{,1} + (\lambda + 2\mu) v_{,2}] |_{x_2=L} = 0 \\ & (u_{,2} + v_{,1}) |_{x_2=L} = 0 \end{aligned} \quad [46]$$

¹⁶¹ Substituting the general solution Eq. 43 into boundary conditions Eqs. 45 and 46, we have

$$\begin{bmatrix} A_1(0) & A_2(0) & A_3(0) & A_4(0) \\ B_1(0) & B_2(0) & B_3(0) & B_4(0) \\ e^{iq_2^1 L} A_1(L) & e^{iq_2^2 L} A_2(L) & e^{iq_2^3 L} A_3(L) & e^{iq_2^4 L} A_4(L) \\ e^{iq_2^1 L} B_1(L) & e^{iq_2^2 L} B_2(L) & e^{iq_2^3 L} B_3(L) & e^{iq_2^4 L} B_4(L) \end{bmatrix} \begin{bmatrix} C_1 \\ C_2 \\ C_3 \\ C_4 \end{bmatrix} = 0 \quad [47]$$

¹⁶³ where $A_i = \lambda q_1 u_i(x_2) + (\lambda + 2\mu) q_2^i v_i(x_2)$, $B_i = q_2^i u_i(x_2) + q_1 v_i(x_2)$. The vanishing of determinant
¹⁶⁴ gives the frequency spectrum for OBC

$$\begin{bmatrix} A_1(0) & A_2(0) & A_3(0) & A_4(0) \\ B_1(0) & B_2(0) & B_3(0) & B_4(0) \\ e^{iq_2^1 L} A_1(L) & e^{iq_2^2 L} A_2(L) & e^{iq_2^3 L} A_3(L) & e^{iq_2^4 L} A_4(L) \\ e^{iq_2^1 L} B_1(L) & e^{iq_2^2 L} B_2(L) & e^{iq_2^3 L} B_3(L) & e^{iq_2^4 L} B_4(L) \end{bmatrix} = 0; \quad [48]$$

¹⁶⁶ also see the red dots in Fig S14A.

¹⁶⁷ Then we turn to derive the GBZ by using the method for the lattice system (7). The solution of
¹⁶⁸ Eq. 48 can be simplified for large L , which forms the corresponding continuum spectrum. Let us
¹⁶⁹ rewrite Eq. 48 with a more general form for the determinant of a $2M$ dimensional matrix

$$\begin{bmatrix} f_1(q_2^1, \omega, \mathcal{S}) & \cdots & f_1(q_2^{2M}, \omega, \mathcal{S}) \\ \vdots & \vdots & \vdots \\ f_M(q_2^1, \omega, \mathcal{S}) & \cdots & f_M(q_2^{2M}, \omega, \mathcal{S}) \\ g_1(q_2^1, \omega, \mathcal{S}) e^{iq_2^1 L} & \cdots & g_1(q_2^{2M}, \omega, \mathcal{S}) e^{iq_2^{2M} L} \\ \vdots & \vdots & \vdots \\ g_M(q_2^1, \omega, \mathcal{S}) e^{iq_2^1 L} & \cdots & g_M(q_2^{2M}, \omega, \mathcal{S}) e^{iq_2^{2M} L} \end{bmatrix} = 0. \quad [49]$$

¹⁷¹ where $M = 2$ for our problem, and \mathcal{S} is the set of the system parameters $\lambda, \mu, \hat{\rho}_{ij}, L$, and q_1 . By
¹⁷² expanding the determinant given in Eq. 49, we have

$$\sum_{P,Q} F(q_2^{i \in P}, q_2^{j \in Q}, \omega, \mathcal{S}) \prod_{l \in P} e^{iq_2^l L} = 0 \quad [50]$$

¹⁷⁴ The sets P and Q are two disjoint subsets of the set $\{1, \dots, 2M\}$ such that the number of elements
¹⁷⁵ of each subset is M . In this way, the sum included in Eq. 48 is taken over all the sets P and Q .

¹⁷⁶ We now consider asymptotic behavior of the solutions of Eq. 50 for large L . When not all of
¹⁷⁷ $\Im(q_y^1), \dots, \Im(q_y^{2M})$ are 0, the only possible solution is $\Im(q_2^M) = \Im(q_2^{M+1})$. If $\Im(q_2^M) \neq \Im(q_2^{M+1})$, there
¹⁷⁸ is only one leading term proportional to $e^{iq_2^{M+1} L} \dots e^{iq_2^{2M} L}$ in Eq. 50 in the limit of a large L . Thus
¹⁷⁹ it leads to

$$F(q_2^{i \in P'}, q_2^{j \in Q'}, \omega, \mathcal{S}) = 0 \quad [51]$$

181 with $P' = \{M + 1, \dots, 2M\}$ and $Q' = \{1, \dots, M\}$. This equation neither depends on L , nor allows
 182 continuum spectrum. On the other hand, when $\Im(q_2^M) = \Im(q_2^{M+1})$, there are two leading terms
 183 proportional to $e^{iq_2^M L} \dots e^{iq_2^{2M} L}$ and to $e^{iq_2^{M+1} L} \dots e^{iq_2^{2M} L}$, and Eq. 50 can be rewritten as

$$184 \quad \frac{e^{iq_2^M L}}{e^{iq_2^{M+1} L}} = -\frac{F(q_2^{i \in P_0}, q_2^{j \in Q_0}, \omega, \mathcal{S})}{F(q_2^{i \in P_1}, q_2^{j \in Q_1}, \omega, \mathcal{S})} \quad [52]$$

185 with $P_0 = \{M + 1, \dots, 2M\}$, $Q_0 = \{1, \dots, M\}$, $P_1 = \{M, M + 2, \dots, 2M\}$, and $Q_1 = \{1, \dots, M - 1, M + 1\}$. In such a case, we can expect that the difference between $\Re(q_2^M)$ and $\Re(q_2^{M+1})$ can be
 186 changed almost continuously for a large L , producing continuum bands.
 187

188 In our case, $\Im(q_2^1) = \dots = \Im(q_2^{2M}) = 0$ just corresponds to a Hermitian situation, and there is no
 189 leading term in Eq. 50. Therefore, we have to solve Eq. (18), completely. However, for Hermitian
 190 situations, $\Re(q_2^1), \dots, \Re(q_2^{2M})$ can change continuously for a large L , and the frequency spectrum is
 191 actually the dispersion curve. Therefore, the frequency spectrum obtained in this case is included in

$$192 \quad \Im(q_2^M) = \Im(q_2^{M+1}), \quad [53]$$

193 with the dispersion relation Eq. 41. Then, we can get the continuous frequency spectrum for both
 194 Hermitian and non-Hermitian cases.

195 By solving Eq. 53 with Eq. 41, we can get the GBZ which are curves in the complex plane; also
 196 see S14B. The GBZ tells us which end the mode is localized at in this study. With the substitution
 197 of the complex wave numbers of the GBZ into the dispersion curve given by Eq. 41, we can get
 198 the PBC spectrum from GBZ; see blue solid line in S14A. We find that the OBC spectrum is same
 199 as the PBC spectrum from GBZ. This suggests the reconstruction of the correspondence between
 200 OBC and PBC spectra based upon the GBZ. Actually, solving Eqs. 53 and 41 not only gives the
 201 GBZ but also gives the frequency spectrum. Therefore, we need not substitute the complex wave
 202 numbers of the GBZ to the dispersion curve.

203 In summary, in order to eliminate the discrepancy between PBC and OBC spectra, wave numbers
 204 should be extended to the GBZ. Meanwhile, we give the simple method to calculate the GBZ without
 205 solving the complete boundary value problem but just using the dispersion relation.

206 **D. Tunable wave manipulation by unbalanced principal mass densities.** Here, we intend to illus-
 207 trate more examples of the tunable wave manipulation functions by the anisotropic principal mass
 208 densities. Taking advantage of the extra degree of freedom from $\hat{\rho}_{11} \neq \hat{\rho}_{22}$, we fix $\hat{\rho}_{11}$ and $\hat{\rho}_{12}$ and
 209 sweep the value of $\hat{\rho}_{22}$. When $\hat{\rho}_{22}/\hat{\rho}_{11}$ is within 0.1 and 2, we plot the normalized divergence and curl
 210 fields of displacement for the selected $\hat{\rho}_{22}/\hat{\rho}_{11}$. Similar to the main text, the stiffness constants of the
 211 odd-mass-density region here are identical to those of the background for good impedance matching.
 212 Examining the steering angles for pressure waves in Figs. S15A-S15F reveals that the numerical
 213 results agree well with the theoretical prediction. Similarly, Examining the steering angles for shear
 214 waves in Figs. S16A-S16F also reveals satisfactory agreement with the theoretical prediction. The
 215 undesired scatterings originate from the impedance mismatch at the interfaces, which can be hardly
 216 removed. Nevertheless, the steered pressure and shear beams enabled by the wave amplification of
 217 odd mass exhibit dominant intensities over the unwanted scatterings, proving the validity of the
 218 functionality of the mass density anisotropy.

219 **Movie S1. Animation with control for transverse incidence.**

220 **Movie S2. Animation without control for transverse incidence.**

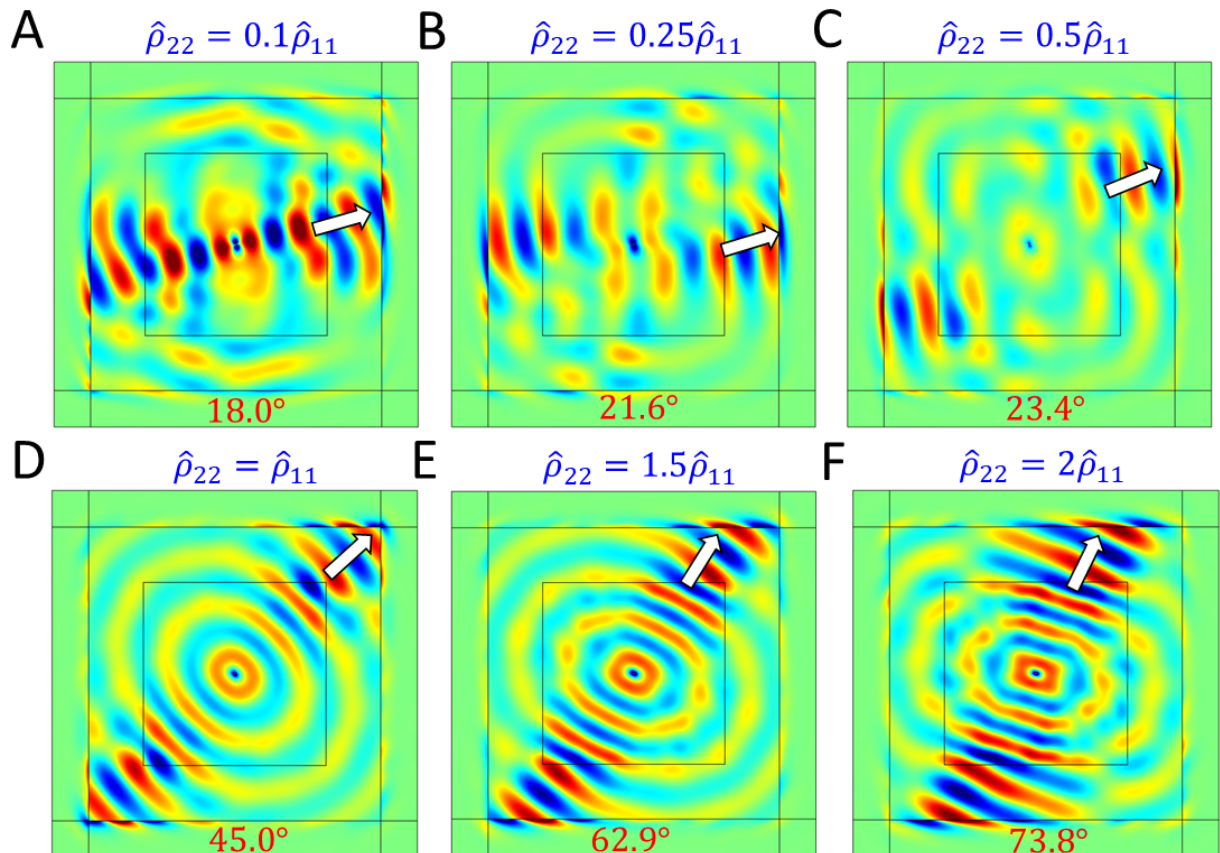


Fig. S15. Pressure wave beam steering with mass density anisotropy in the presence of odd mass density. (A-F) Normalized divergence fields of displacement when $\hat{\rho}_{22}/\hat{\rho}_{11}$ takes 0.1, 0.25, 0.5, 1, 1.5 and 2. The background media are the same as the previous. While the stiffness properties of the odd mass regions are consistent with that of the background for better impedance matching. In all field plots, $\hat{\rho}_{11}$ and β are fixed at 16277 kg/m^3 and 0.6144, respectively. All the field intensities are normalized with their respective maximums at 16 kHz. On the bottom of each field plot, the theoretical principal direction angle θ_1 for the maximum amplification rate is indicated in red.

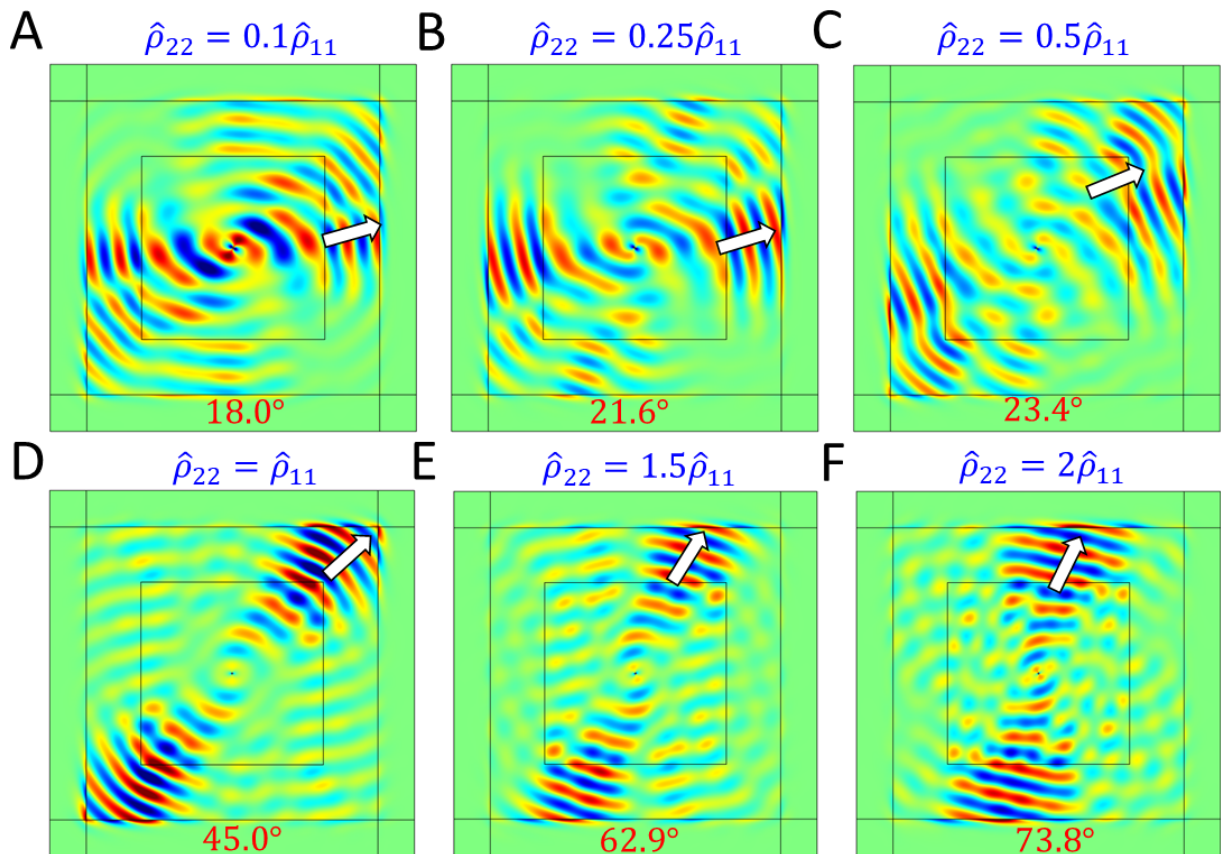


Fig. S16. Shear wave beam steering with mass density anisotropy in the presence of odd mass density. (A-F) Normalized curl fields of displacement when $\hat{\rho}_{22}/\hat{\rho}_{11}$ takes 0.1, 0.25, 0.5, 1, 1.5 and 2. The background media are the same as the previous. While the stiffness properties of the odd mass regions are consistent with that of the background for better impedance matching. In all field plots, $\hat{\rho}_{11}$ and $\hat{\beta}$ are fixed at 16277 kg/m^3 and 0.6144, respectively. All the field intensities are normalized with their respective maximums at 16 kHz. On the bottom of each field plot, the theoretical principal direction angle θ_1 for the maximum amplification rate is indicated in red.

²²¹ Movie S3. Time-dependent 2D simulations.

²²² Movie S4. Time-dependent 2D measurement.

²²³ References

- ²²⁴ 1. X Liu, G Hu, C Sun, G Huang, Wave propagation characterization and design of two-dimensional elastic chiral metacomposite. *J. Sound Vib.* **330**, 2536–2553 (2011).
- ²²⁵ 2. Y Wu, Y Lai, ZQ Zhang, Effective medium theory for elastic metamaterials in two dimensions. *Phys. Rev. B* **76**, 205313 (2007).
- ²²⁶ 3. Y Lai, Y Wu, P Sheng, ZQ Zhang, Hybrid elastic solids. *Nat. materials* **10**, 620–624 (2011).
- ²²⁷ 4. Q Wu, G Huang, Omnidirectional wave polarization manipulation in isotropic polar solids. *Int. J. Solids Struct.* **241**, 111481 (2022).
- ²²⁸ 5. H Nassar, Y Chen, G Huang, Isotropic polar solids for conformal transformation elasticity and cloaking. *J. Mech. Phys. Solids* **129**, 229–243 (2019).
- ²²⁹ 6. Q Wu, X Zhang, P Shivashankar, Y Chen, G Huang, Independent flexural wave frequency conversion by a linear active metalayer. *Phys. Rev. Lett.* **128**, 244301 (2022).
- ²³⁰ 7. K Yokomizo, S Murakami, Non-bloch band theory of non-hermitian systems. *Phys. review letters* **123**, 066404 (2019).